IR-improved DGLAP parton shower effects in $W+$ jets in pp collisions at $\sqrt{s}=7$ TeV

B. Shakerin* and B. F. L. Ward†

Physics Department, Baylor University, Waco, Texas 76798-7316, USA

(Received 17 July 2018; revised manuscript received 8 February 2019; published 27 August 2019)

We use HERWIRI1.031, a new Monte Carlo event generator for hadron-hadron scattering at high energies, to study the phenomenological effects of our approach of exact amplitude-based resummation in precision QCD calculations. $W+$ jet(s) events with exact NLO QCD corrections are generated in the MG5_aMC@NLO framework and showered by both HERWIRI1.031 and HERWIG6.5 with PTRMS $=0$ and PTRMS $=2.2$ GeV$/c$, respectively. Here, PTRMS is the rms value of the intrinsic Gaussian transverse momentum distribution for the partons inside the proton. The differential cross sections for many observables are presented, such as the jet rapidities and the jet transverse momenta as well as other event observables such as the scalar sums of transverse momenta of the jets, the missing transverse energy of the jets and the dijets' observables. Finally, we compare our results with the ATLAS and CMS measurements of the W production cross sections in association with jets.

DOI: 10.1103/PhysRevD.100.034026

I. INTRODUCTION

In the precision theory of the Standard Model (SM), since we are dealing with the computation of the higher order Feynman diagrams in which the virtual and real radiative corrections are involved, the treatment of the ultraviolet (UV), infrared (IR), and collinear singularities plays a crucial role. The UV singularities appear in the virtual diagrams and are removed by renormalization [1–3]. The soft (IR) and collinear singularities appear in theories with massless particles. The IR singularities are removed at the first order of perturbative expansion by the Bloch-Nordsieck approach [4]. The most general treatment of the IR singularities was developed by Yennie-Frautschi-Suura (YFS) [5,6]. The main feature of the YFS approach is based on the separation of the infrared divergences as multiplicative exponentiated factors, which are treated exactly to all orders of perturbation theory, and the conversion of the residual exact perturbation expansion into one that has no infrared divergence and, hence, no need for an infrared cutoff. The significant advantage of the YFS formalism is that it is exact to all orders in the QED coupling constant. The YFS formalism was developed and extended by one of us, B.F.L.W., to the non-Abelian gauge theories [7–9]. One can show that the exact, amplitude-based resummation leads to the IR improvement of the usual DGLAP-CS theory [10–13], which results in a new set of kernels, parton distributions, and attendant reduced cross sections, so that the QCD perturbative results for the respective hadron-hadron or lepton-hadron cross section are unchanged order by order in α_s at large squared-momentum transfers. This IR-improved behavior, for example, results in kernels that are integrable in the IR limit and therefore are more amenable to realization by the Monte Carlo (MC) method [14–20] to arbitrary precision. The advantage of this IR-improved method is better control on the accuracy of a given fixed-order calculation throughout the entire phase space of the respective physical process, especially when the prediction is given by the MC method. This new approach seems important, especially in the era of LHC, in which we must deal with the requirements of precision QCD, which involves predictions for QCD processes at the total precision tag of 1% or better.

In this paper, we extend the studies in Refs. [14–20], which were focused on the single Z/γ^* production at FNAL and LHC, to the single W production at the LHC, with the additional change that we look into the properties of jets, produced in association with the W, in relation to the physics of IR-improved DGLAP-CS kernels. We study whether the manifestation of the IR-improved kernels as seen in the decay lepton observables in Refs. [14–20] will also be seen in the distributions of jet observables. We thus focus on the processes $pp \to \mathrm{W}+n$ jets, $n=1, 2, 3$. We use the MG5_aMC@NLO [21] framework into which we have introduced the Herwiri1.031 [14–20] IR-improved shower to be compared with the standard unimproved

*bahram_shakerin@baylor.edu
†bfl_ward@baylor.edu

Herwig6.5 [22] shower in that framework. In this way, we realize exact next-to-leading-order (NLO) matrix element matched parton showers with and without IR improvement. We compare with the data from ATLAS and CMS at 7 TeV to make contact with observations.

The paper is organized as follows. In the next section we give a brief review of exact QED ⊗ QCD resummation theory. In Sec. III we describe our event generation, analysis, and cuts. In Sec. IV we compare our predictions with the ATLAS 7 TeV data. In Sec. V we compare our predictions with the CMS 7 TeV data. Section VI contains our concluding remarks.

II. EXTENSION OF YFS THEORY TO QED ⊗ QCD

We start with a prototypical process $pp\to W^{\pm}+n(\gamma)+m(g)+X\to l^{\pm}+\nu_{l^{\pm}}+n'(\gamma)+m(g)+X'$, where $l=\{e,\mu\}$, $\nu_{l^+}=\nu_l$, and $\nu_{l^-}=\bar{\nu}_l$. The new QED ⊗ QCD YFS extension is obtained by simultaneously resumming the large IR terms in QCD and the IR dominant terms in QED. One can prove that the exponentiated cross section is given by [23–27]

$$\begin{aligned}d\hat{\sigma}_{\rm exp}&=\sum_{n=0}^{\infty}d\tilde{\sigma}^n=e^{{\rm SUM_{IR}(QCED)}}\sum_{n,m=0}^{\infty}\int\prod_{j_1=1}^{n}\frac{d^3k_{j1}}{k_{j1}}\prod_{j_2=1}^{m}\frac{d^3k'_{j2}}{k'_{j2}}\\&\times\int\frac{d^4y}{(2\pi)^4}e^{iy\cdot((p_1+q_1-p_2-q_2-\sum k_{j1}-\sum k'_{j2})+D_{\rm QCED}}\\&\times\tilde{\bar{\beta}}_{n,m}(k_1,\ldots,k_n;k'_1,\ldots,k'_m)\frac{d^3p_2}{p_2^0}\frac{d^3q_2}{q_2^0},\end{aligned}\tag{1}$$

with $n(\gamma)$ hard photons and $m(g)$ hard gluons, where $\tilde{\bar{\beta}}_{n,m}(k_1,\ldots,k_n;k'_1,\ldots,k'_m)$ are the YFS residuals that are free of all infrared divergences to all orders in α_s and α. The infrared functions are given by

$${\rm SUM_{IR}(QCED)}=2\alpha_s{\rm Re}B^{nls}_{\rm QCED}+2\alpha_s\tilde{B}^{nls}_{\rm QCED}(K_{\rm max}),\tag{2}$$

$$2\alpha_s\tilde{B}_{\rm QCED}(K_{\rm max})=\int\frac{d^3k}{k^0}\tilde{S}^{nls}_{\rm QCED}(k)\theta(K_{\rm max}-k),\tag{3}$$

$$D_{\rm QCED}=\int\frac{d^3k}{k}\tilde{S}^{nls}_{\rm QCED}(k)[e^{-iy\cdot k}-\theta(K_{\rm max}-k)],\tag{4}$$

and the functions ${\rm SUM_{IR}(QCED)}$ and $D_{\rm QCED}$ are determined from their QCD analogs ${\rm SUM_{IR}(QCD)}$ and $D_{\rm QCD}$ via the following substitutions:

$$\begin{cases}B^{nls}_{\rm QCD}\to B^{nls}_{\rm QCD}+B^{nls}_{\rm QED}\equiv B^{nls}_{\rm QCED},\\ \tilde{B}^{nls}_{\rm QCD}\to\tilde{B}^{nls}_{\rm QCD}+\tilde{B}^{nls}_{\rm QED}\equiv\tilde{B}^{nls}_{\rm QCED},\\ \tilde{S}^{nls}_{\rm QCD}\to\tilde{S}^{nls}_{\rm QCD}+\tilde{S}^{nls}_{\rm QED}\equiv\tilde{S}^{nls}_{\rm QCED}.\end{cases}\tag{5}$$

In Eq. (5), the superscript nls asserts that the infrared functions $B_{\rm QCD}$, $B_{\rm QED}$, $\tilde{B}_{\rm QCD}$, $\tilde{B}_{\rm QED}$, and $\tilde{S}_{\rm QCD}$ are DGLAP-CS synthesized. These infrared functions have been introduced in Refs. [28–31]. The QCD exponentiation of the master formula in Eq. (1) leads to a new set of IR-improved splitting functions listed:

$$\begin{cases}P^{\rm exp}_{qq}(z)=C_Fe^{\frac{1}{2}\delta_q}F_{\rm YFS}(\gamma_q)\left[\frac{1+z^2}{1-z}(1-z)^{\gamma_q}-f_q(\gamma_q)\delta(1-z)\right],\\ P^{\rm exp}_{Gq}(z)=C_Fe^{\frac{1}{2}\delta_q}F_{\rm YFS}(\gamma_q)\frac{1+(1-z)^2}{z}z^{\gamma_q},\\ P^{\rm exp}_{qG}(z)=e^{\frac{1}{2}\delta_q}F_{\rm YFS}(\gamma_q)\frac{1}{2}\{z^2(1-z)^{\gamma_G}+(1-z)^2z^{\gamma_G}\},\\ P^{\rm exp}_{GG}(z)=2C_GF_{\rm YFS}(\gamma_G)e^{\frac{1}{2}\delta_G}\Big\{\frac{1-z}{z}z^{\gamma_G}+\frac{z}{1-z}(1-z)^{\gamma_G}\\ +\frac{1}{2}((1-z)z^{\gamma_G+1}+z(1-z)^{\gamma_G+1})-f_G(\gamma_G)\delta(1-z)\Big\},\end{cases}\tag{6}$$

where

$$\begin{cases}\gamma_q=C_F\frac{\alpha_s}{\pi}t=\frac{4C_F}{\beta_0},\qquad\delta_q=\frac{\gamma_q}{2}+\frac{\alpha_sC_F}{\pi}\left(\frac{\pi^2}{3}-\frac{1}{2}\right),\\ \gamma_G=C_G\frac{\alpha_s}{\pi}t=\frac{4C_G}{\beta_0},\qquad\delta_G=\frac{\gamma_G}{2}+\frac{\alpha_sC_G}{\pi}\left(\frac{\pi^2}{3}-\frac{1}{2}\right),\\ F_{\rm YFS}(x)=\frac{e^{C_Ex}}{\Gamma(1+x)},\qquad\beta_0=11-\frac{2}{3}n_f=4\beta_1,\\ C_E=0.57721566\ldots,\\ f_q(\gamma_q)=\frac{2}{\gamma_q}-\frac{2}{\gamma_q+1}+\frac{1}{\gamma_q+2},\\ \bar{f}_G(\gamma_G)=\frac{n_f}{C_G}\frac{1}{(1+\gamma_G)(2+\gamma_G)(3+\gamma_G)}+\frac{2}{\gamma_G(1+\gamma_G)(2+\gamma_G)}\\ \qquad+\frac{1}{(1+\gamma_G)(2+\gamma_G)}+\frac{1}{2(3+\gamma_G)(4+\gamma_G)}+\frac{1}{(2+\gamma_G)(3+\gamma_G)(4+\gamma_G)}\end{cases}\tag{7}$$

Finally, for precision LHC theory, the famous factorization theorem [32]

$$\sigma=\sum_{i,j}\int dx_1dx_2F_i(x_1)F_j(x_2)\hat{\sigma}(x_1x_2s)\tag{8}$$

is written in the following form:

$$\sigma=\sum_{i,j}\int dx_1dx_2F'_i(x_1)F'_j(x_2)\hat{\sigma}'(x_1x_2s),\tag{9}$$

where the primed quantities are associated with the kernels and cross sections derived in Eqs. (6) and (1), respectively. The implementation of the new IR-improved kernels in the HERWIG6.5 [22] environment leads to a new MC, HERWIRI1.031, as described in Ref. [33]. In what follows, we present results using both the original HERWIG6.5 and the new IR-improved HERWIRI1.031. For both MG5_aMC@NLO/HERWIG and MG5_aMC@NLO/HERWIRI simulations, we use the NNPDF2.3nlo PDFs [34].

III. EVENT GENERATION, ANALYSIS, AND CUTS

The generators for $W+$ jet events are MADGRAPH5_aMC@NLO [21] interfaced with HERWIG6.521 and HERWIRI1.031, which use with exact NLO matrix element calculations matched to the respective parton shower. The number of events generated for the W, $W+1$ jet, $W+2$ jet, and $W+3$ jet processes are 10^7, 10^6, 10^5, and 10^5, respectively. These events are showered by MADGRAPH5_aMC@NLO/HERWIRI1.031 [35] (PTRMS = 0) and MADGRAPH5_aMC@NLO/HERWIG6.521 (PTRMS = 2.2 GeV) [36]. During the analysis, jets were reconstructed using the anti-k_t algorithm with FastJet [37] and the cuts in Tables I and II were imposed for the ATLAS and CMS results, respectively.

The transverse mass, m_T, is defined as $m_T = \sqrt{2P_T^l P_T^{\nu_l}(1-\cos\Delta\phi)}$ where $\Delta\phi$ is the difference in the azimuthal angle between the direction of the lepton momentum and the associated neutrino, ν_l, which can be written as

$$\Delta\phi = \phi^l - \phi^{\nu_l}. \tag{10}$$

Rapidity is defined as $\frac{1}{2}\ln[\frac{E+p_z}{E-p_z}]$, where E denotes the energy of the particle and p_z is the longitudinal component of the momentum. Finally, the jet isolation, ΔR, which is a Lorentz invariant quantity for massless particles, is defined as

$$\Delta R(l,\text{jet}) = \sqrt{\Delta\phi^2(l,\text{jet}) + \Delta\eta^2(l,\text{jet})}, \tag{11}$$

where

$$\begin{cases} \Delta\phi(l,\text{jet}) = \phi_l - \phi_{\text{jet}}, \\ \Delta\eta(l,\text{jet}) = \eta_l - \eta_{\text{jet}}, \\ \eta = -\ln\tan\left(\frac{\theta}{2}\right), \end{cases} \tag{12}$$

where θ is the angle between the respective particle three-momentum $\vec{P}$ and the positive direction of the beam axis. The E_T^{miss} is calculated as the negative vector sum of the transverse momenta of calibrated leptons, photons, and jets and additional low-energy deposits in the calorimeter.

TABLE I. Kinematic criteria defining the fiducial phase space for the $W \to l + \nu_l$ channel.

Combined channel $W \to l + \nu_l$ where $l = \{e, \mu\}$	
Lepton P_T^l	$P_T^l > 25$ GeV
Lepton rapidity η_l	$\lvert\eta_l\rvert < 2.5$
Missing transverse energy	$E_T^{\text{miss}} > 25$ GeV
Transverse mass	$m_T > 40$ GeV
Jet algorithm	Anti-k_T
Radius parameter R	$R = 0.4$
Jet P_T^{jet}	$P_T^{\text{jet}} > 30$ GeV
Jet rapidity Y_{jet}	$\lvert Y_{\text{jet}}\rvert < 4.4$
Jet isolation	$\Delta R(l,\text{jet}) > 0.5$ (jet is removed)

TABLE II. Kinematic criteria defining the fiducial phase space for the $W \to \mu + \nu_\mu$ channel.

Muon channel ($W \to \mu + \nu_\mu$)	
Lepton P_T^μ	$P_T^\mu > 25$ GeV
Lepton rapidity η_μ	$\lvert\eta_\mu\rvert < 2.1$
Missing transverse energy	$E_T^{\text{miss}} > 25$ GeV
Transverse mass	$m_T > 50$ GeV
Jet algorithm	Anti-k_t
Radius parameter R	$R = 0.5$
Jet P_T^{jet}	$P_T^{\text{jet}} > 30$ GeV
Jet pseudorapidity η_{jet}	$\lvert\eta_{\text{jet}}\rvert < 2.4$
Jet isolation	$\Delta R(\mu,\text{jet}) > 0.5$ (jet is removed)

IV. RESULTS (ATLAS COLLABORATION)

In this section, the measured $W(\to l + \nu_l) +$ jets fiducial cross sections [38] are shown and compared to the predictions of MADGRAPH5_aMC@NLO/HERWIRI1.031 and MADGRAPH5_aMC@NLO/HERWIG6.521. Each distribution is combined separately by minimizing a χ^2 function. The factors applied to the theory predictions are summarized in Appendix A and Appendix B (see Tables III and IV). We have used the following notation throughout this paper:

(i) herwiri ≡ MADGRAPH5_aMC@NLO/HERWIRI1.031 (PTRMS = 0);
(ii) herwig ≡ MADGRAPH5_aMC@NLO/HERWIG6.521 (PTRMS = 2.2 GeV).

A. Transverse momentum distributions

The differential cross sections as a function of the leading jet transverse momentum are shown in Figs. 1 and 2 for the $W+ \geq 1$ jet and $W+1$ jet cases, respectively. In both cases, there is agreement between the data and predictions provided by HERWIRI and HERWIG in the soft regime.

In Fig. 1, for $P_T < 140$ GeV, HERWIRI predictions are in better agreement with the data, where $(\frac{\chi^2}{\text{d.o.f}})_{\text{HERWIRI}} = 0.76$ and $(\frac{\chi^2}{\text{d.o.f}})_{\text{HERWIRI}} = 2.04$. The $(\frac{\chi^2}{\text{d.o.f}})$ functions have been calculated for the first nine bins. In Fig. 2, for $P_T < 120$ GeV, $(\frac{\chi^2}{\text{d.o.f}})_{\text{HERWIRI}} = 1.13$ and $(\frac{\chi^2}{\text{d.o.f}})_{\text{HERWIRI}} = 0.96$. The $(\frac{\chi^2}{\text{d.o.f}})$ functions have been calculated for the first eight bins. For the sake of clarification, the ratio plots for Figs. 1 and 2 are given in Appendix C. In the ratio plot, each point represents $\frac{\text{Data}}{\text{Theory}}$ (see Figs. 41–49).

The differential cross sections for the production of $W+ \geq 2$ jets as a function of the leading jet P_T and the second leading jet P_T are shown in Figs. 3 and 4,

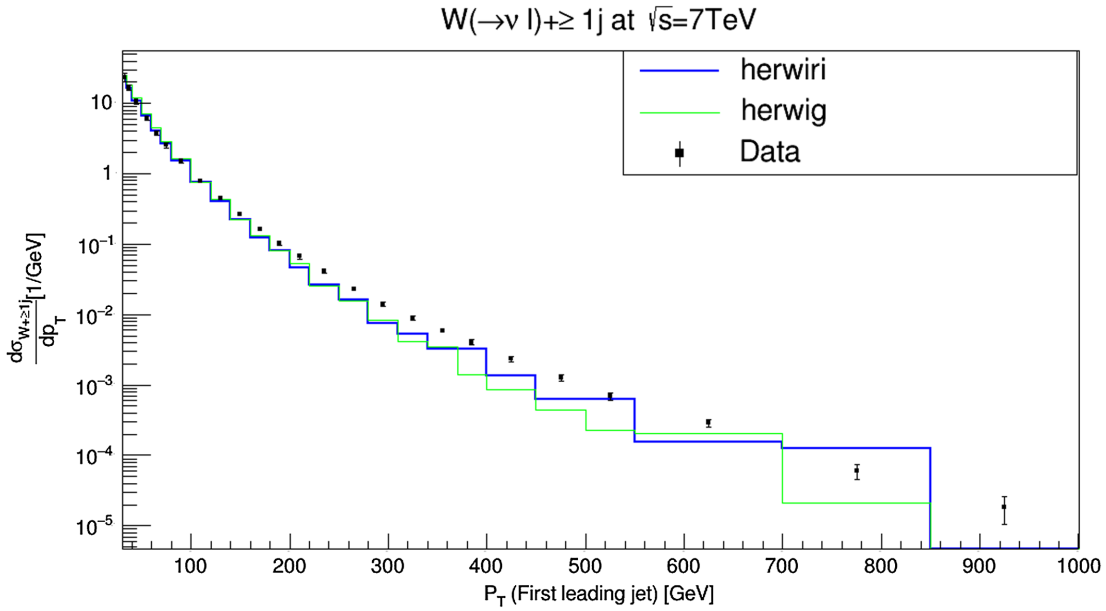

FIG. 1. Cross section for the production of $W+$jets as a function of the leading-jet P_T in $N_{\text{jet}} \geq 1$. The data are compared to predictions from MADGRAPH5_aMC@NLO/HERWIRI1.031 and MADGRAPH5_aMC@NLO/HERWIG6.521.

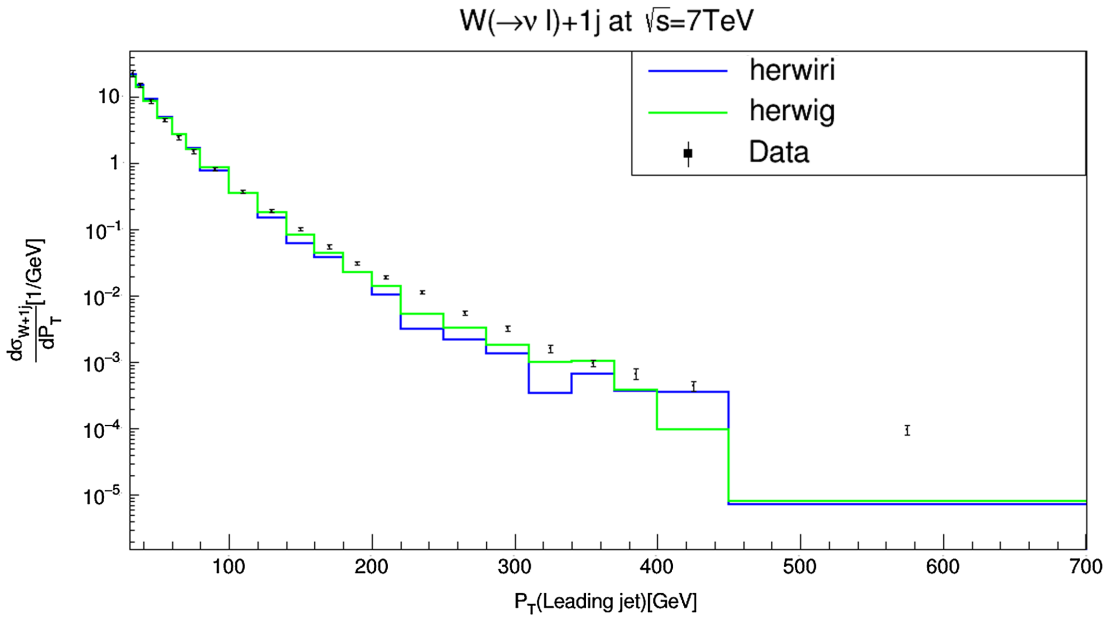

FIG. 2. Cross section for the production of $W+$jets as a function of the leading-jet P_T in $N_{\text{jet}} = 1$. The data are compared to predictions from MADGRAPH5_aMC@NLO/HERWIRI1.031 and MADGRAPH5_aMC@NLO/HERWIG6.521.

respectively. HERWIRI and HERWIG generally describe the data well for $P_T < 200$ GeV. In Fig. 3, $(\frac{\chi^2}{\text{d.o.f}})_{\text{HERWIRI}} = 1.19$ and $(\frac{\chi^2}{\text{d.o.f}})_{\text{HERWIRI}} = 1.49$, while for $200 < P_T < 350$ GeV it seems that they both fail to describe the data. For $250 < P_T < 550$ GeV, HERWIRI predictions overlap with the data while HERWIG either underestimates or overestimates the data. Finally, for energies higher than 550 GeV, they both underestimate the data. The behaviors for $P_T > 200$ GeV are consistent with our theoretical curves' exact NLO matrix element (ME) matched parton shower precision.

Figure 4 shows that HERWIRI, in general, gives a better fit to the data for $P_T < 150$ GeV, where $(\frac{\chi^2}{\text{d.o.f}})_{\text{HERWIRI}} = 1.06$ and $(\frac{\chi^2}{\text{d.o.f}})_{\text{HERWIRI}} = 1.69$. For higher P_T, in some

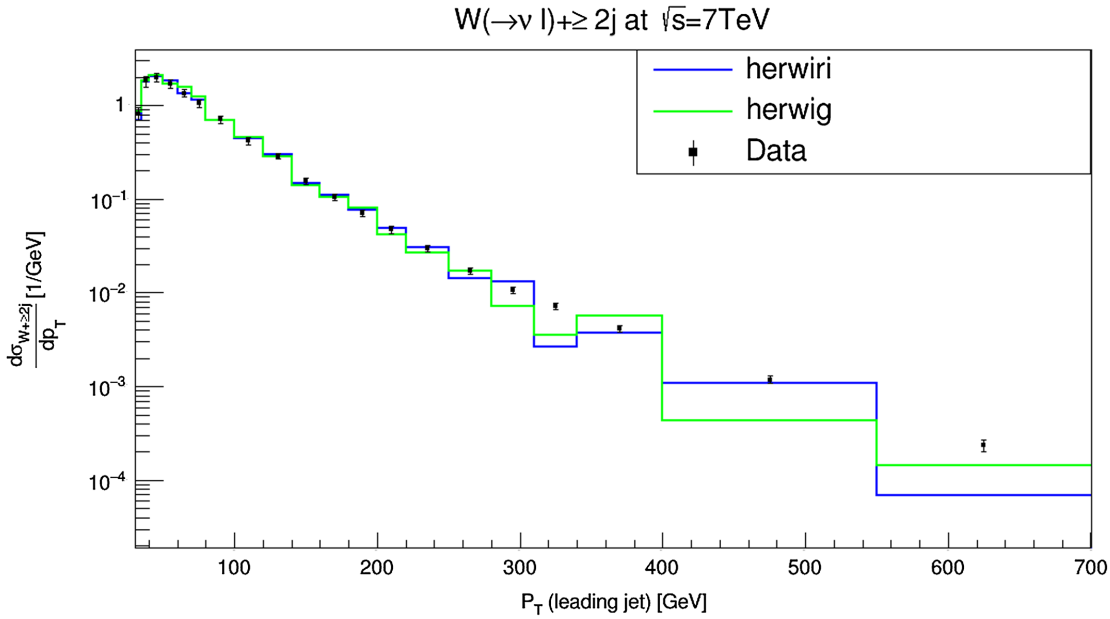

FIG. 3. Cross section for the production of $W+$jets as a function of the leading-jet P_T in $N_{\text{jet}} \geq 2$. The data are compared to predictions from MADGRAPH5_aMC@NLO/HERWIRI1.031 and MADGRAPH5_aMC@NLO/HERWIG6.521.

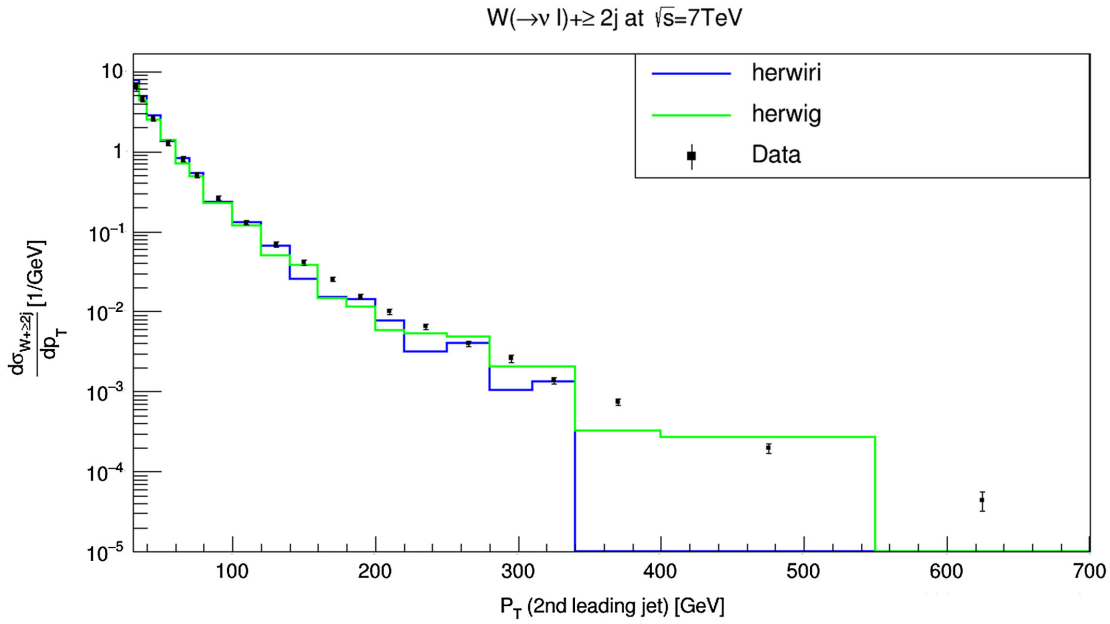

FIG. 4. Cross section for the production of $W+$jets as a function of the second leading-jet P_T in $N_{\text{jet}} \geq 2$. The data are compared to predictions from MADGRAPH5_aMC@NLO/HERWIRI1.031 and MADGRAPH5_aMC@NLO/HERWIG6.521.

cases HERWIRI predictions overlap with the data while HERWIG either underestimates or overestimates the data. We conclude that HERWIRI gives a better fit to the data in the soft regime as expected. The differential cross sections for the production of $W+\geq 3$ jets as a function of the leading jet P_T and the third leading jet P_T are shown in Figs. 5 and 6, respectively. In Fig. 5, for $P_T < 150$ GeV, the predictions provided by HERWIRI and HERWIG are in complete agreement with the data, where $(\frac{\chi^2}{\text{d.o.f}})_{\text{HERWIRI}} = 0.27$ and $(\frac{\chi^2}{\text{d.o.f}})_{\text{HERWIRI}} = 0.20$. For $P_T > 150$ GeV, HERWIG gives a better fit to the data while HERWIRI underestimates the data. In Fig. 6, HERWIRI gives a better fit to the data for low P_T, $P_T < 150$ GeV, where

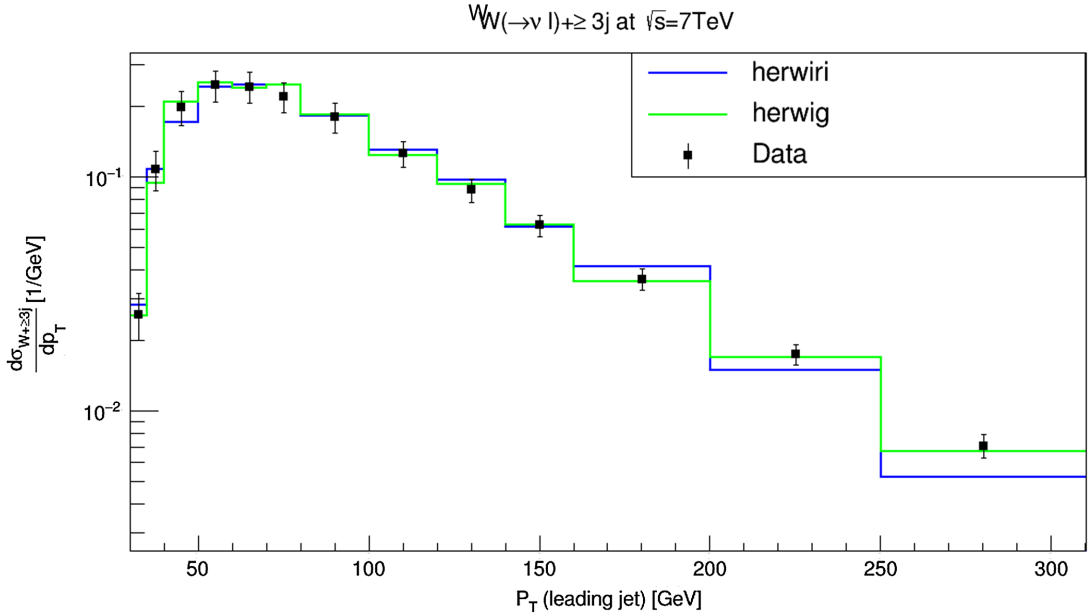

FIG. 5. Cross section for the production of $W+$jets as a function of the leading-jet P_T in $N_{\text{jet}} \geq 3$. The data are compared to predictions from MADGRAPH5_aMC@NLO/HERWIRI1.031 and MADGRAPH5_aMC@NLO/HERWIG6.521.

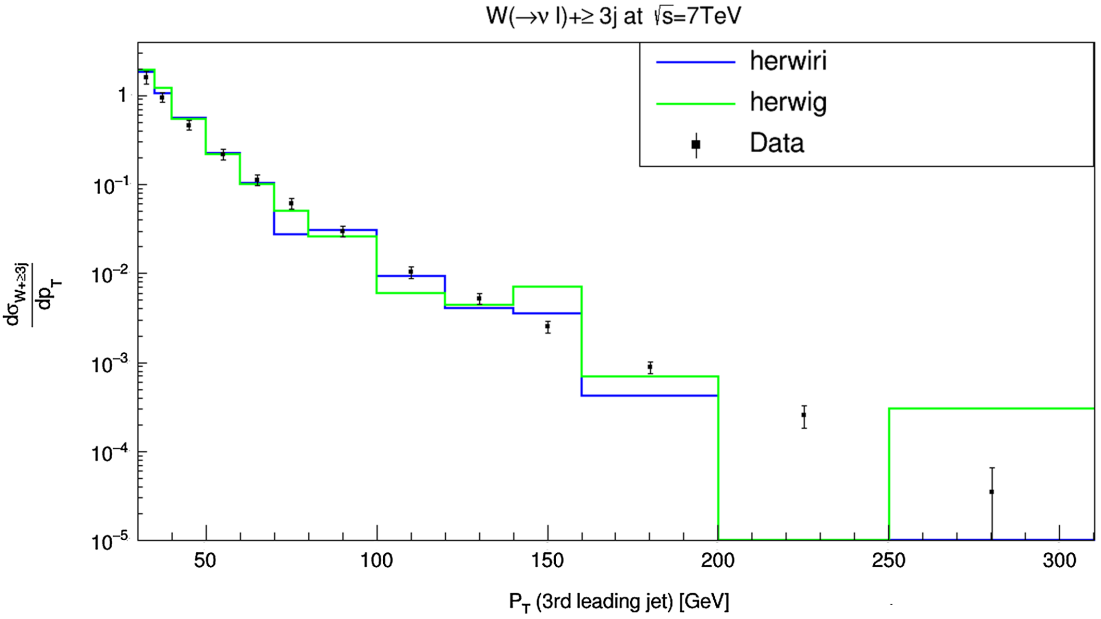

FIG. 6. Cross section for the production of $W+$jets as a function of the third leading-jet P_T in $N_{\text{jet}} \geq 3$. The data are compared to predictions from MADGRAPH5_aMC@NLO/HERWIRI1.031 and MADGRAPH5_aMC@NLO/HERWIG6.521.

$(\frac{\chi^2}{\text{d.o.f}})_{\text{HERWIRI}} = 3.27$ and $(\frac{\chi^2}{\text{d.o.f}})_{\text{HERWIRI}} = 3.97$. For large P_T, in almost all cases HERWIRI and HERWIG predictions either underestimate or overestimate the data.

In general, one could conclude that the predictions provided by HERWIRI give as good a fit or a better fit to the data for soft P_T without the need of an *ad hoc* intrinsic Gaussian rms transverse momentum of 2.2 GeV as needed by HERWIG.

B. Rapidity distributions

The differential cross sections for the production of the $W+\geq 1$ jet as a function of the leading jet Y_j are shown in Fig. 7. The predictions provided by HERWIRI and HERWIG are generally in agreement with the data, although in three cases HERWIRI predictions overlap with the data while the HERWIG predictions either underestimate or overestimate the data. We clearly conclude that HERWIRI

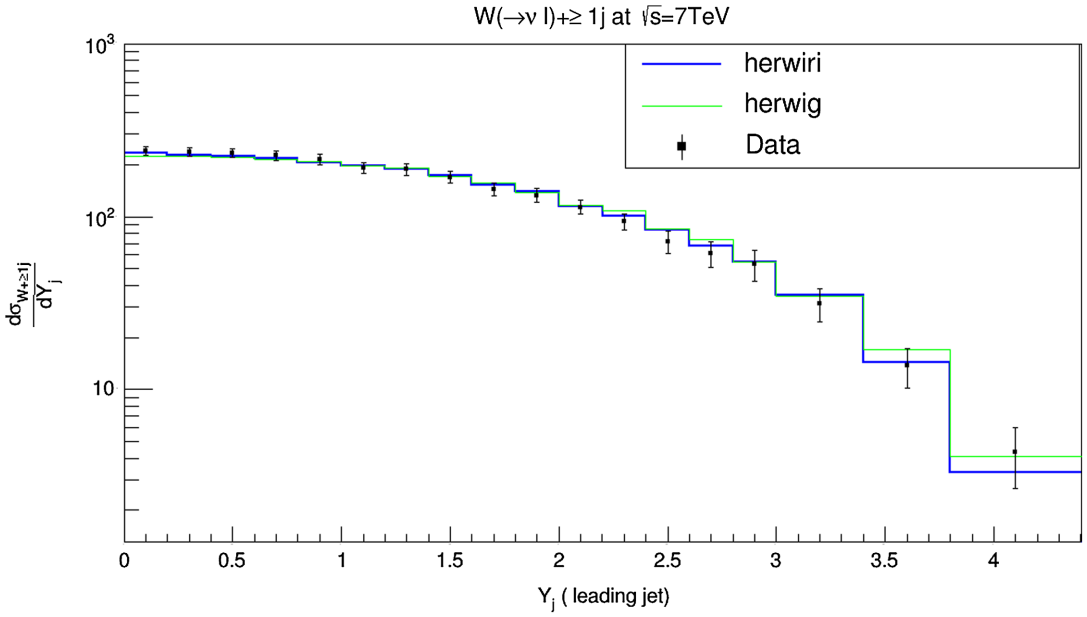

FIG. 7. Cross section for the production of W + jets as a function of the leading-jet Y_j in $N_{\text{jet}} \geq 1$. The data are compared to predictions from MADGRAPH5_aMC@NLO/HERWIRI1.031 and MADGRAPH5_aMC@NLO/HERWIG6.521.

and HERWIG give a very good fit to the data with $(\frac{\chi^2}{\text{d.o.f}})_{\text{HERWIRI}} = 0.35$ and $(\frac{\chi^2}{\text{d.o.f}})_{\text{HERWIRI}} = 0.70$.

The differential cross sections for the production of $W+ \geq 2$ jets as a function of the second leading jet Y_j are shown in Fig. 8. The results provided by HERWIRI and HERWIG overlap with the data in almost all cases. In two cases the HERWIRI predictions overlap with the data, and in two cases the HERWIG results overlap with the data while HERWIRI predictions either underestimate or overestimate the data: $(\frac{\chi^2}{\text{d.o.f}})_{\text{HERWIRI}} = 1.01$ and $(\frac{\chi^2}{\text{d.o.f}})_{\text{HERWIRI}} = 0.63$. Here, both theoretical predictions give acceptable fits to the data.

The differential cross sections for the production of $W+ \geq 3$ jets as a function of the third leading jet Y_j are

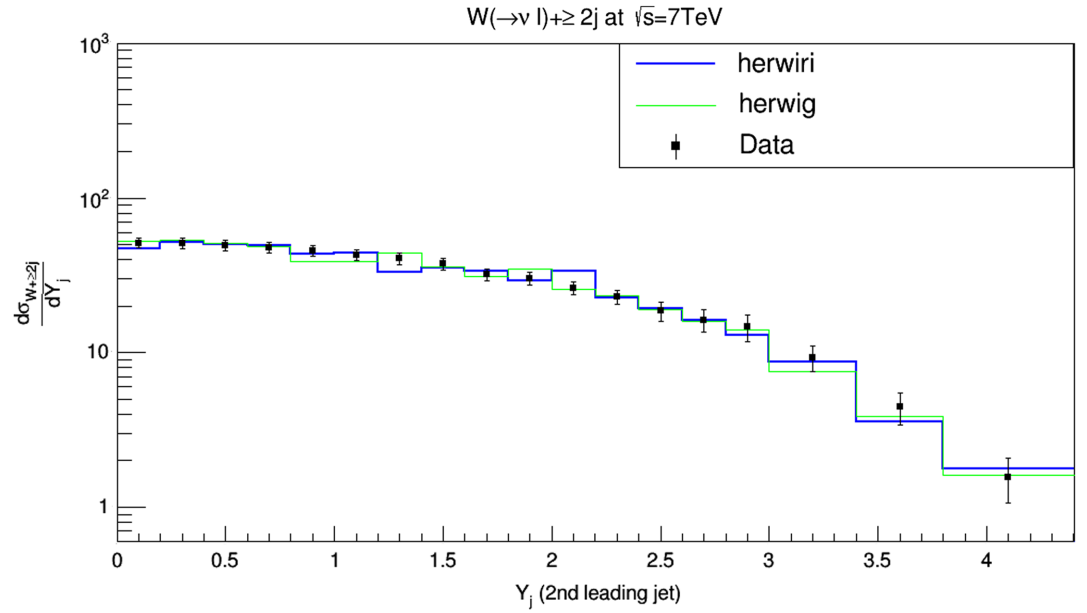

FIG. 8. Cross section for the production of W + jets as a function of the second leading-jet Y_j in $N_{\text{jet}} \geq 2$. The data are compared to predictions from MADGRAPH5_aMC@NLO/HERWIRI1.031 and MADGRAPH5_aMC@NLO/HERWIG6.521.

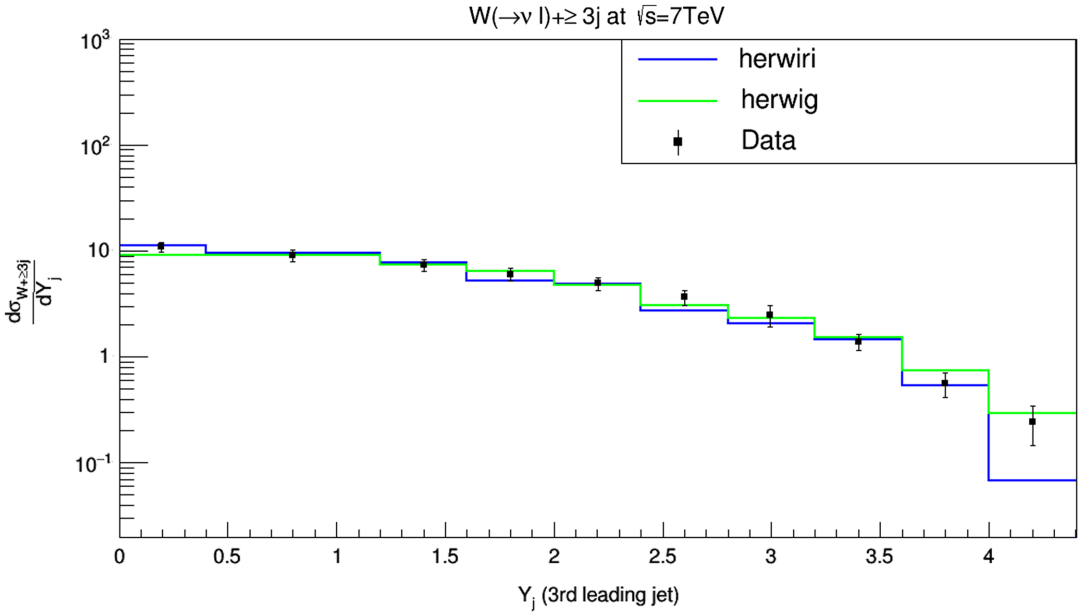

FIG. 9. Cross section for the production of $W+$ jets as a function of the third leading-jet Y_j in $N_{\rm jet} \geq 3$. The data are compared to predictions from MADGRAPH5_aMC@NLO/HERWIRI1.031 and MADGRAPH5_aMC@NLO/HERWIG6.521.

shown in Fig. 9. For $Y_j < 3.6$, with the exception of one case in which only the HERWIG prediction overlaps with the error bars on the data, HERWIRI and HERWIG predictions are in agreement with the data. For $Y_j > 3.6$, in one case HERWIRI overlaps with the error bars on the data while HERWIG overestimates the data, and in the other case HERWIG overlaps with the error bars on the data while HERWIRI underestimates the data $(\frac{\chi^2}{\rm d.o.f})_{\rm HERWIRI} = 1.05$ and $(\frac{\chi^2}{\rm d.o.f})_{\rm HERWIRI} = 0.43$ so that both predictions give acceptable fits to the data.

C. Dijet angular variables, invariant mass, separation

In this subsection the differential cross sections are shown as functions of the difference in azimuthal angle ($\Delta\phi_{j_1,j_2}$), the difference in the rapidity ($\Delta Y_{j_1,j_2}$), the angular separation ($\Delta R_{j_1,j_2}$), and the dijet invariant mass (m_{j_1,j_2}) in comparison to the data. We define the aforementioned variables as follows:

$$\Delta Y_{j_1,j_2} = |Y_{j_1} - Y_{j_2}|, \tag{13}$$

$$\Delta\phi_{j_1,j_2} = |\phi_{j_1} - \phi_{j_2}|, \tag{14}$$

$$\Delta R_{j_1,j_2} = \sqrt{(\Delta\phi_{j_1,j_2})^2 + \Delta\eta_{j_1,j_2})^2}, \tag{15}$$

$$\begin{aligned} M_{j_1,j_2} &= \sqrt{(E_{j_1} + E_{j_2})^2 - (\vec{P}_{j_1} + \vec{P}_{j_2})^2} \\ &= \sqrt{m_{j_1}^2 + m_{j_2}^2 + 2(E_{j_1}E_{j_2} - \vec{P}_{j_1}\cdot\vec{P}_{j_2})}. \end{aligned} \tag{16}$$

We note that in Eq. (15), $\Delta\eta_{j_1,j_2}$ is the difference in pseudorapidity [39] of the first and second leading jets. The ith jet is defined as

$$P^{\mu}_{\rm ith-jet} = (E_{j_1}, \vec{P}_{\rm ith-jet}). \tag{17}$$

The differential cross sections for the production of $W+ \geq 2$ jets as a function of the dijet invariant mass between the two leading jets are shown in Fig. 10. The cross sections are fairly well modeled by HERWIRI for $M_{j_1,j_2} < 300$ GeV. For $M_{j_1,j_2} > 300$ GeV there are cases in which HERWIRI gives a good fit to the data while HERWIG predictions either underestimate or overestimate the data. In comparison, predictions provided by HERWIRI describe the data somewhat better than do those provided by HERWIG: $(\frac{\chi^2}{\rm d.o.f})_{\rm HERWIRI} = 1.18$ and $(\frac{\chi^2}{\rm d.o.f})_{\rm HERWIRI} = 1.69$ for $M_{j_1,j_2} < 300$ GeV.

The differential cross sections for the production of $W+ \geq 2$ jets as a function of the difference in the rapidity between the two leading jets are shown in Fig. 11. For $\Delta Y_{j_1,j_2} < 3$ the predictions provided by HERWIRI give a better fit to the data. For $3 < \Delta Y_{j_1,j_2} < 4$, HERWIG results provide a better description of the data $(\frac{\chi^2}{\rm d.o.f})_{\rm HERWIRI} = 2.08$ and $(\frac{\chi^2}{\rm d.o.f})_{\rm HERWIRI} = 4.77$, so that overall HERWIRI gives a better fit to the data.

The differential cross sections for the production of $W+ \geq 2$ jets as a function of the angular separation between the two leading jets are shown in Fig. 12. For $\Delta R_{j_1,j_2} > 3$, the cross sections are fairly well modeled by the predictions of HERWIRI and HERWIG. For $\Delta R_{j_1,j_2} < 3$, in at least two cases the prediction provided

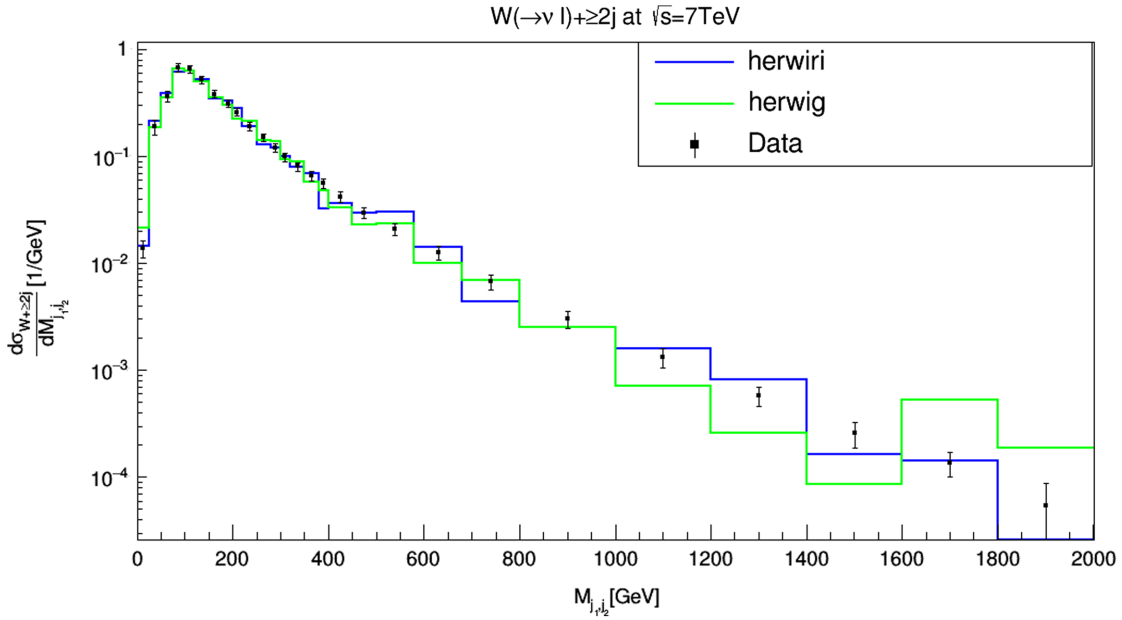

FIG. 10. Cross section for the production of $W+$jets as a function of the dijet invariant mass m_{j_1,j_2} between the two leading jets in $N_{\text{jet}} \geq 2$. The data are compared to predictions from MADGRAPH5_aMC@NLO/HERWIRI1.031 and MADGRAPH5_aMC@NLO/HERWIG6.521.

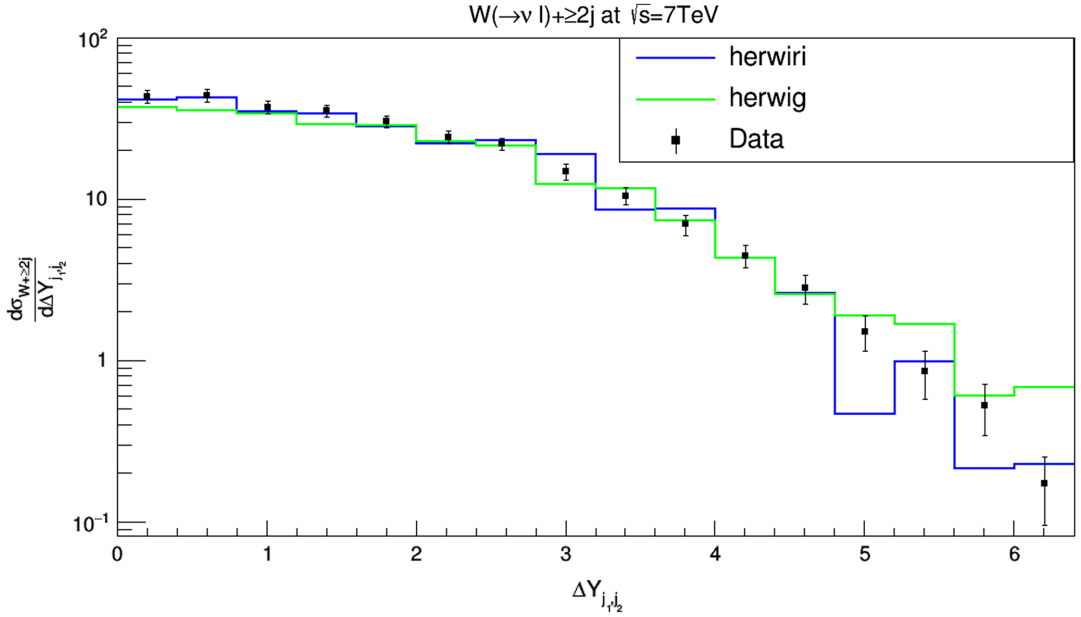

FIG. 11. Cross section for the production of $W+$jets as a function of the difference in the rapidity between the two leading jets in $N_{\text{jet}} \geq 2$. The data are compared to predictions from MADGRAPH5_aMC@NLO/HERWIRI1.031 and MADGRAPH5_aMC@NLO/HERWIG6.521.

by either of them is outside of the error bars on the data; in most cases they both give a satisfactory prediction relative to the data: $(\frac{\chi^2}{\text{d.o.f}})_{\text{HERWIRI}}=1.59$ and $(\frac{\chi^2}{\text{d.o.f}})_{\text{HERWIRI}} = 0.78$.

The differential cross sections for the production of $W+\geq 2$ jets as a function of the azimuthal angle between the two leading jets are shown in Fig. 13. For $\Delta\phi_{j_1,j_2} < 0.4$, $1 < \Delta\phi_{j_1,j_2} < 1.4$, and $\Delta\phi_{j_1,j_2} > 2.2$, the predicted cross

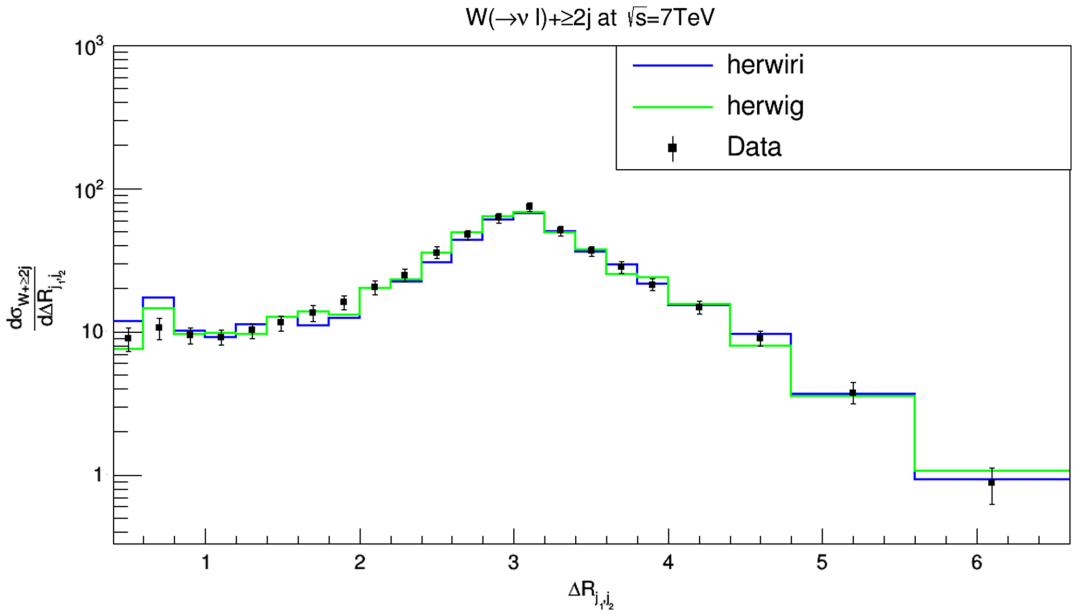

FIG. 12. Cross section for the production of $W+$ jets as a function of the angular separation between the two leading jets for $N_{\text{jet}} \geq 2$. The data are compared to predictions from MADGRAPH5_aMC@NLO/HERWIRI1.031 and MADGRAPH5_aMC@NLO/HERWIG6.521.

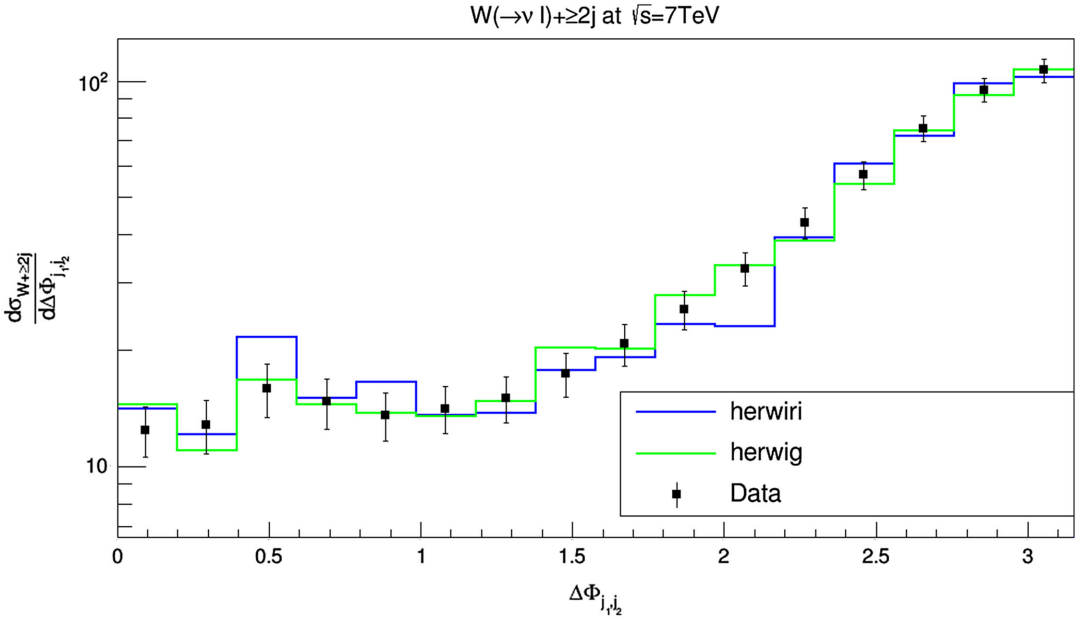

FIG. 13. Cross section for the production of $W+$ jets as a function of the difference in the azimuthal angle between the two leading jets in $N_{\text{jet}} \geq 2$. The data are compared to predictions from MADGRAPH5_aMC@NLO/HERWIRI1.031 and MADGRAPH5_aMC@NLO/HERWIG6.521.

sections by HERWIRI and HERWIG are within the error bars on the data: $(\frac{\chi^2}{\text{d.o.f}})_{\text{HERWIRI}} = 1.46$ and $(\frac{\chi^2}{\text{d.o.f}})_{\text{HERWIRI}} = 0.49$, so that, while both predictions give acceptable fits to the data, the HERWIG fit is the better one.

D. Scalar sum H_T

In this subsection we will study the $W+$ jets cross sections as a function of H_T, the summed scalar P_T of all

identified objects in the final state. For example, for a prototypical process

$$pp \to l + \nu_l + j_1 + j_2, \tag{18}$$

we define H_T as follows:

$$H_T = P_T(l) + P_T(\nu_l) + P_T(j_1) + P_T(j_2), \tag{19}$$

where $l = e, \mu$.

The differential cross sections as a function of H_T are shown in Figs. 14–19, respectively. We will study the $W +$ jets cross sections as a function of H_T for low H_T. We will

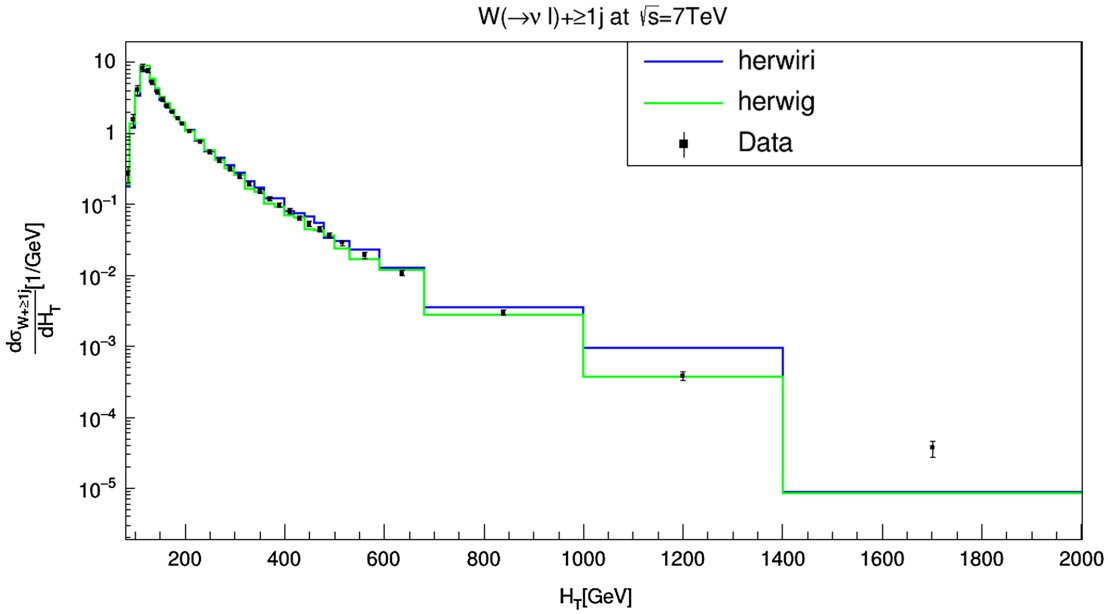

FIG. 14. Cross section for the production of $W +$ jets as a function of the scalar sum H_T in $N_{\text{jet}} \geq 1$. The data are compared to predictions from MADGRAPH5_aMC@NLO/HERWIRI1.031 and MADGRAPH5_aMC@NLO/HERWIG6.521.

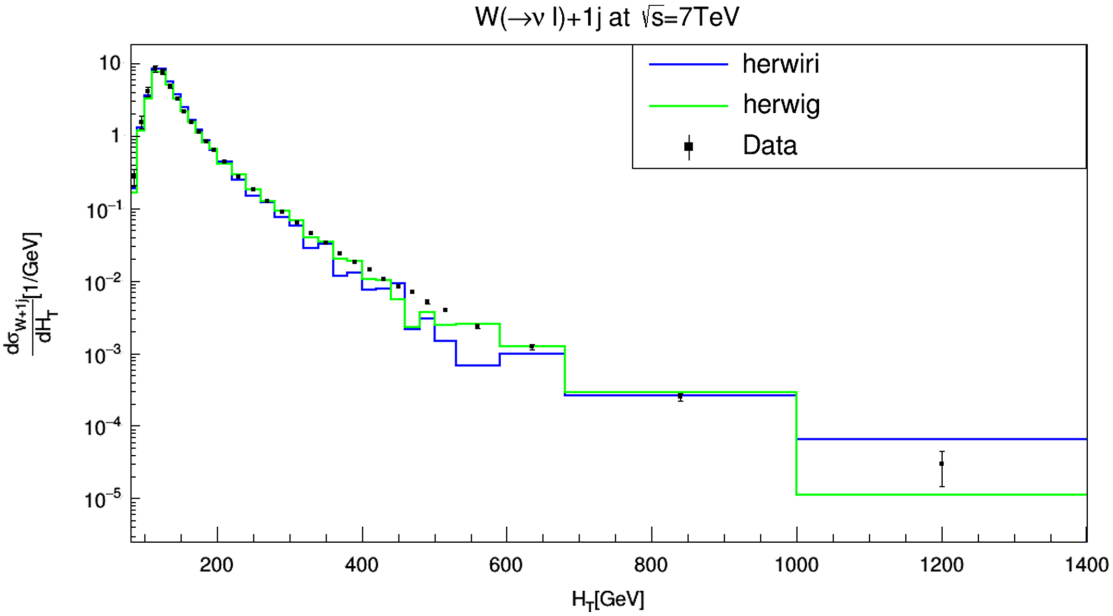

FIG. 15. Cross section for the production of $W +$ jets as a function of the scalar sum H_T in $N_{\text{jet}} = 1$. The data are compared to predictions from MADGRAPH5_aMC@NLO/HERWIRI1.031 and MADGRAPH5_aMC@NLO/HERWIG6.521.

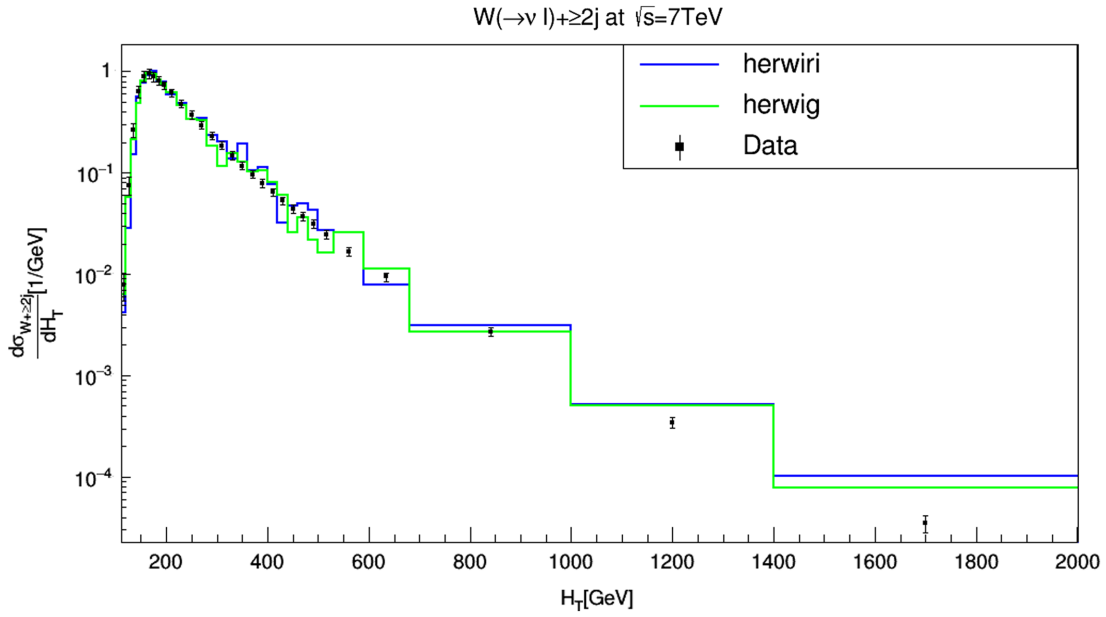

FIG. 16. Cross section for the production of $W+$ jets as a function of the scalar sum H_T in $N_{\text{jet}} \geq 2$. The data are compared to predictions from MADGRAPH5_aMC@NLO/HERWIRI1.031 and MADGRAPH5_aMC@NLO/HERWIG6.521.

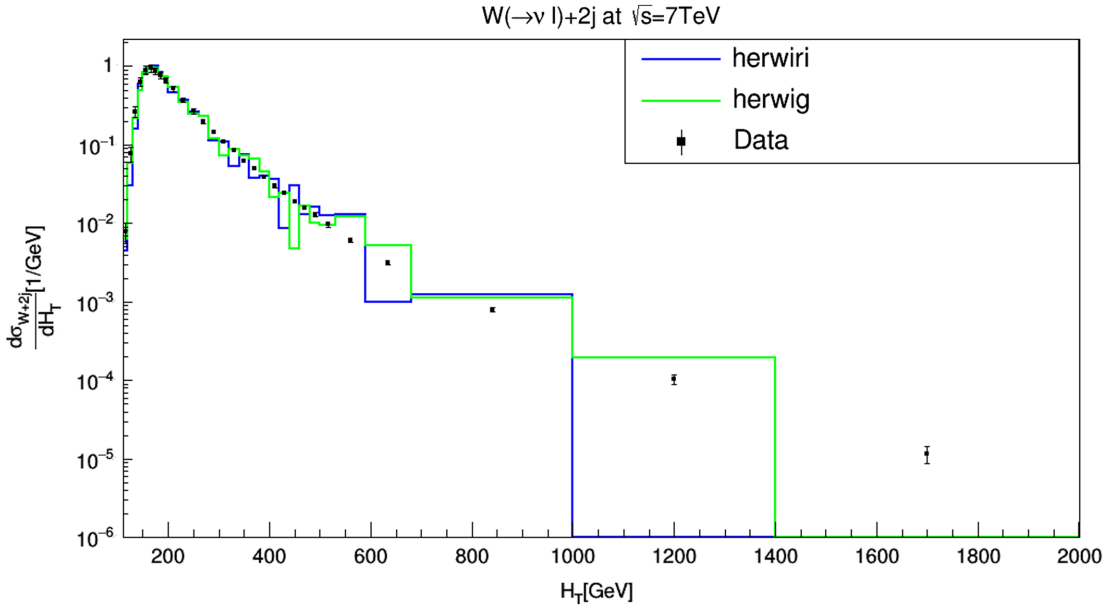

FIG. 17. Cross section for the production of W + jets as a function of the scalar sum H_T in $N_{\text{jet}} = 2$. The data are compared to predictions from MADGRAPH5_aMC@NLO/HERWIRI1.031 and MADGRAPH5_aMC@NLO/HERWIG6.521.

see in some cases HERWIRI predictions are in agreement with the data and in some cases HERWIG predictions give a better fit to the data. In general, a better agreement is provided for the lower jet multiplicities, e.g., $W+1$ jet and $W+\geq 1$ jet.

The differential cross sections for the production of the $W+\geq 1$ jet as a function of the scalar sum H_T are shown in Fig. 14. For $H_T < 300$ GeV, HERWIRI and HERWIG predictions are in good agreement with data where $(\frac{\chi^2}{\text{d.o.f}})_{\text{HERWIRI}} = 0.591$ and $(\frac{\chi^2}{\text{d.o.f}})_{\text{HERWIRI}} = 0.96$. For

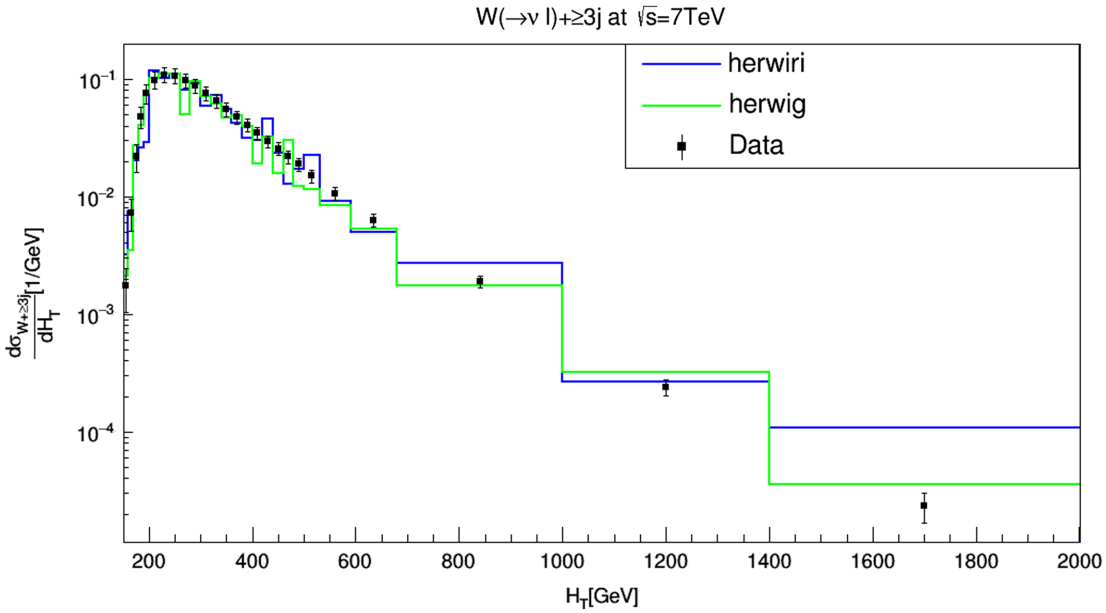

FIG. 18. Cross section for the production of $W+$ jets as a function of the scalar sum H_T in $N_{\text{jet}} \geq 3$. The data are compared to predictions from MADGRAPH5_aMC@NLO/HERWIRI1.031 and MADGRAPH5_aMC@NLO/HERWIG6.521.

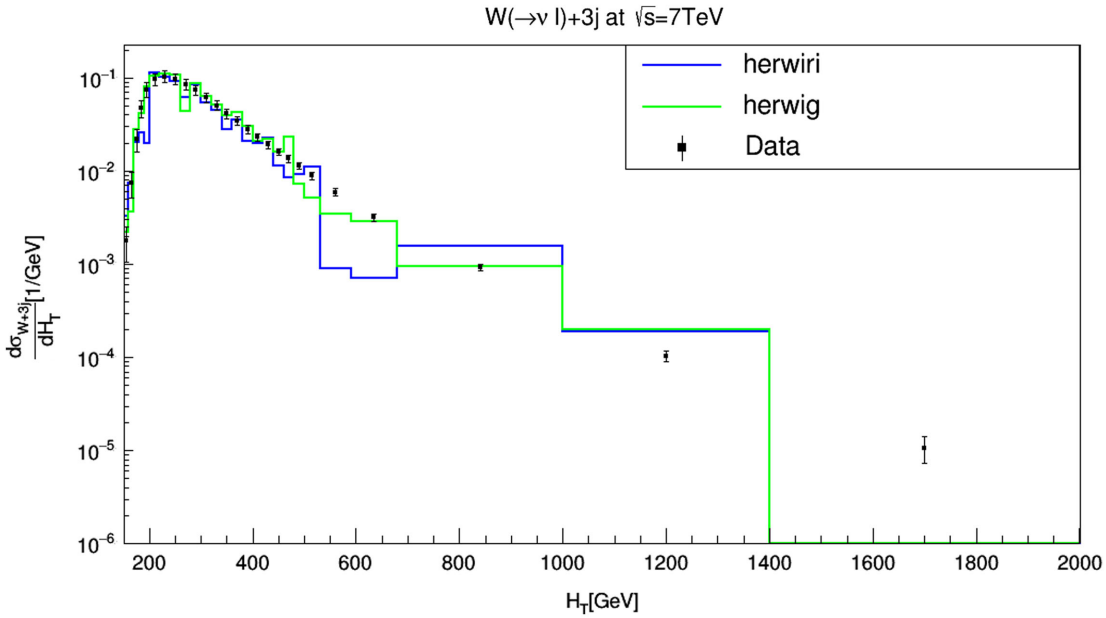

FIG. 19. Cross section for the production of $W+$ jets as a function of the scalar sum H_T in $N_{\text{jet}} = 3$. The data are compared to predictions from MADGRAPH5_aMC@NLO/HERWIRI1.031 and MADGRAPH5_aMC@NLO/HERWIG6.521.

$400 < H_T < 1400$ GeV, the differential cross sections are fairly well modeled by the HERWIG predictions. (See Appendix C.)

The differential cross sections for the production of $W+1$ jet as a function of the scalar sum H_T are shown in Fig. 15. For the case $H_T < 275$ GeV, HERWIG predictions are in better agreement with the data while the predictions provided by HERWIRI either overestimate or underestimate the data in some cases: $(\frac{\chi^2}{\text{d.o.f}})_{\text{HERWIRI}} = 3.50$ and $(\frac{\chi^2}{\text{d.o.f}})_{\text{HERWIRI}} = 0.76$. For $275 < H_T < 1000$ GeV, the differential cross sections are fairly well modeled by HERWIG predictions. HERWIRI predictions in almost all cases underestimate the data for $275 < H_T < 1000$ GeV.

(See Appendix C.) The differential cross sections for the production of $W+ \geq 2$ jets as a function of the scalar sum H_T are shown in Fig. 16. The predictions provided by HERWIG give a better fit to the data in $H_T < 275$ GeV, with $(\frac{\chi^2}{\text{d.o.f}})_{\text{HERWIRI}} = 2.25$ and $(\frac{\chi^2}{\text{d.o.f}})_{\text{HERWIRI}} = 1.26$. In the $275 < H_T < 450$ GeV range, HERWIRI gives a better fit to the data; in the $450 < H_T < 650$ GeV range, HERWIG predictions are in better agreement with the data. For large H_T, HERWIG predictions either are in agreement with the data or have less discrepancy with the data than the results provided by HERWIRI, as Fig. 16 reveals.

The differential cross sections for the production of $W + 2$ jets as a function of the scalar sum H_T are shown in Fig. 17. HERWIRI and HERWIG seem to be unable to provide a good fit for the data at $H_T < 190$ GeV where they underestimate the data. In the $H_T < 250$ GeV range, HERWIG predictions are in better agreement with the data, where $(\frac{\chi^2}{\text{d.o.f}})_{\text{HERWIRI}} = 2.36$ and $(\frac{\chi^2}{\text{d.o.f}})_{\text{HERWIRI}} = 1.09$.

At scalar sum values around $170 < H_T < 250$ GeV, HERWIRI and HERWIG predictions overlap fairly well with the data. In general, we conclude that the discrepancy of the predictions provided by HERWIRI is less than that of HERWIG.

The differential cross sections for the production of $W+ \geq 3$ jets as a function of the scalar sum H_T are shown in Fig. 18. A good fit is provided by the HERWIG predictions for $H_T < 275$ GeV, where $(\frac{\chi^2}{\text{d.o.f}})_{\text{HERWIRI}} = 2.71$ and $(\frac{\chi^2}{\text{d.o.f}})_{\text{HERWIRI}} = 2.01$. The HERWIG and HERWIRI predictions overlap fairly well with the data for $275 < H_T < 400$ GeV. For the higher range $650 < H_T < 2000$ GeV, the HERWIG predictions are in better agreement with the data while in most cases HERWIRI either underestimates or overestimates the data.

The differential cross sections for the production of $W + 3$ jets as a function of the scalar sum H_T are shown in Fig. 19. HERWIG gives a better fit to the data for $H_T < 250$, with $(\frac{\chi^2}{\text{d.o.f}})_{\text{HERWIRI}} = 3.73$ and $(\frac{\chi^2}{\text{d.o.f}})_{\text{HERWIRI}} = 0.79$. In general, the predictions provided by HERWIG give a better fit to the data.

E. Scalar sum S_T

In this subsection, we study the behavior of $W +$ jets cross sections as a function of the scalar sum S_T, where S_T is defined as the summed scalar P_T of all the jets in the event:

$$S_T = \sum_{i=1}^{N\text{jet}} |P_T(i)|, \tag{20}$$

where $|P_T(i)|$ is the transverse momentum of the ith jet and Njet is the maximum number of jets in each event. The differential cross sections as a function of S_T are shown in Figs. 20–24, respectively. We will study the $W +$ jets cross sections as a function of S_T for low S_T. We will see in some cases HERWIRI predictions are in agreement with the data and in some cases HERWIG predictions give a better fit to the data. In general, a better agreement is provided for the lower jet multiplicities, e.g., $W + 1$ jet and $W+ \geq 1$ jet.

The differential cross sections for the production of $W+ \geq 1$ jet as a function of the scalar sum S_T are shown in Fig. 20. A good fit to the data is provided by HERWIRI at $S_T < 300$ GeV while HERWIG predictions

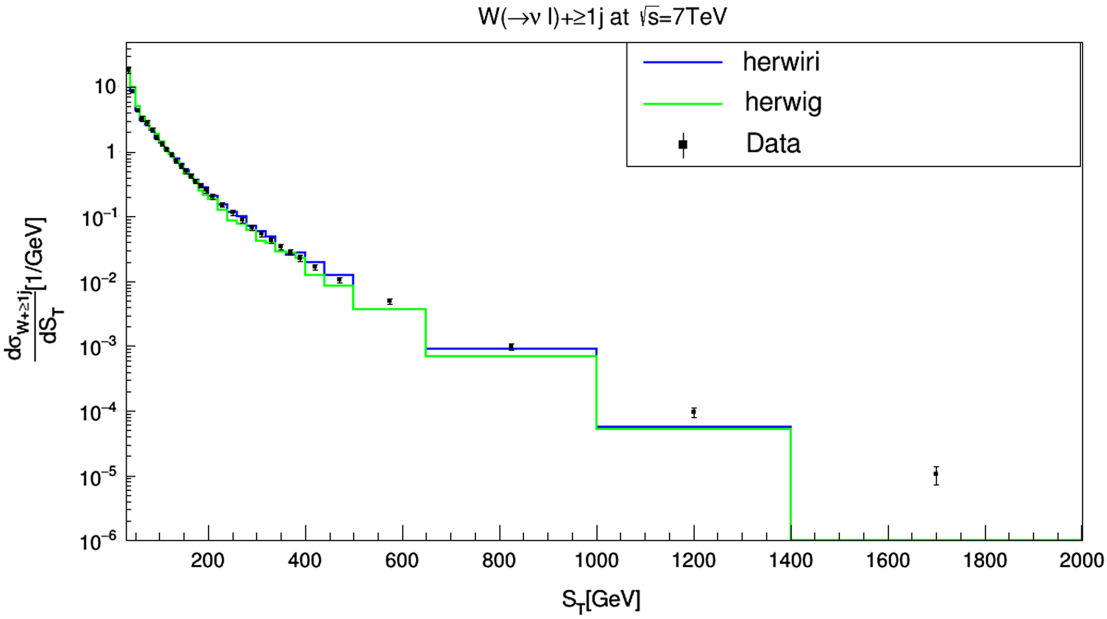

FIG. 20. Cross section for the production of $W +$ jets as a function of the scalar sum S_T in $N_{\text{jet}} \geq 1$. The data are compared to predictions from MADGRAPH5_aMC@NLO/HERWIRI1.031 and MADGRAPH5_aMC@NLO/HERWIG6.521.

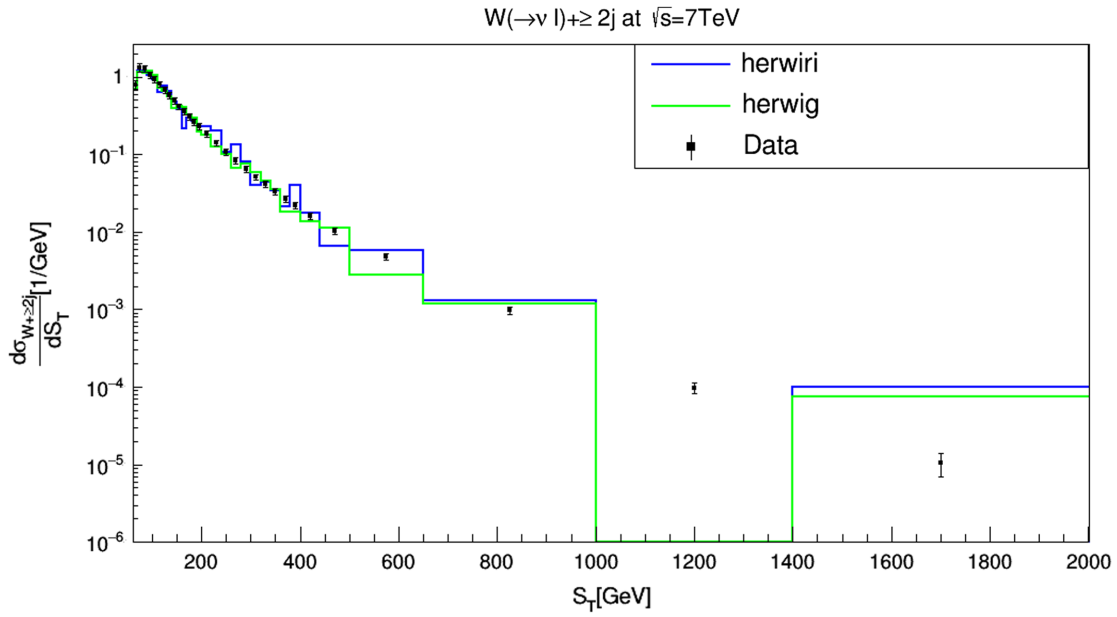

FIG. 21. Cross section for the production of $W+$jets as a function of the scalar sum S_T in $N_{\text{jet}} \geq 2$. The data are compared to predictions from MADGRAPH5_aMC@NLO/HERWIRI1.031 and MADGRAPH5_aMC@NLO/HERWIG6.521.

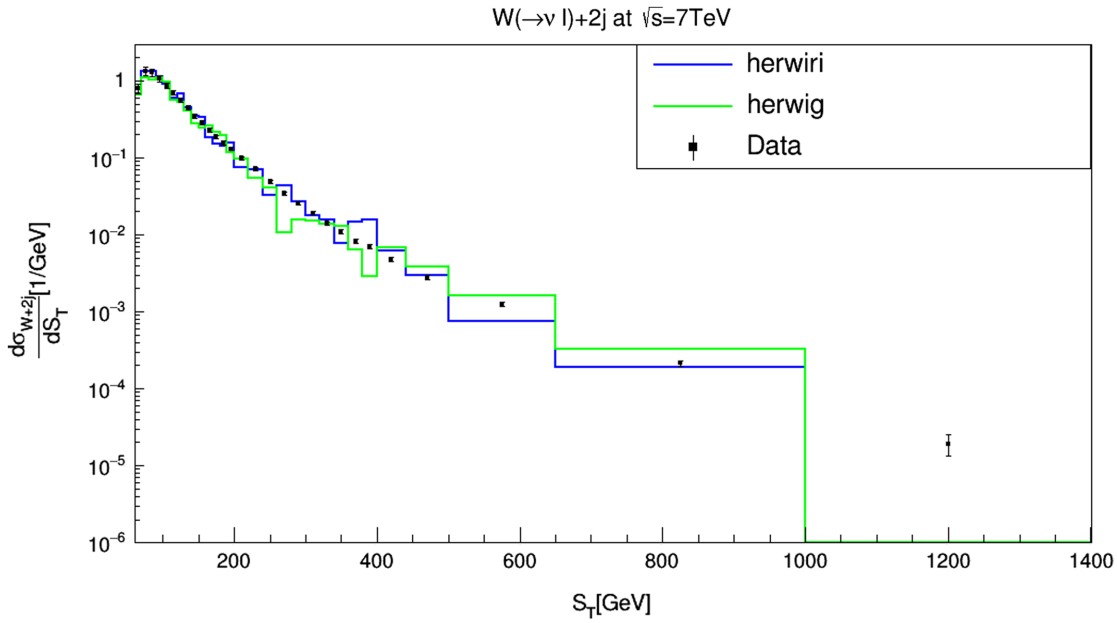

FIG. 22. Cross section for the production of $W+$jets as a function of the scalar sum S_T in $N_{\text{jet}} = 2$. The data are compared to predictions from MADGRAPH5_aMC@NLO/HERWIRI1.031 and MADGRAPH5_aMC@NLO/HERWIG6.521.

lie below the data in some cases: $(\frac{\chi^2}{\text{d.o.f}})_{\text{HERWIRI}} = 0.28$ and $(\frac{\chi^2}{\text{d.o.f}})_{\text{HERWIRI}} = 1.94$. For $300 < S_T < 1000$ GeV, the HERWIRI predictions are in good agreement with the data. For higher values of S_T, $1000 < S_T < 2000$ GeV, HERWIRI and HERWIG predictions underestimate the data.

The differential cross sections for the production of $W+ \geq 2$ jets as a function of the scalar sum S_T are shown in Fig. 21. For $S_T < 200$ GeV, the predictions provided by HERWIG are in better agreement with the data: $(\frac{\chi^2}{\text{d.o.f}})_{\text{HERWIRI}} = 2.96$ and $(\frac{\chi^2}{\text{d.o.f}})_{\text{HERWIRI}} = 1.65$. For medium values of S_T, the HERWIG predictions give a fair fit to the

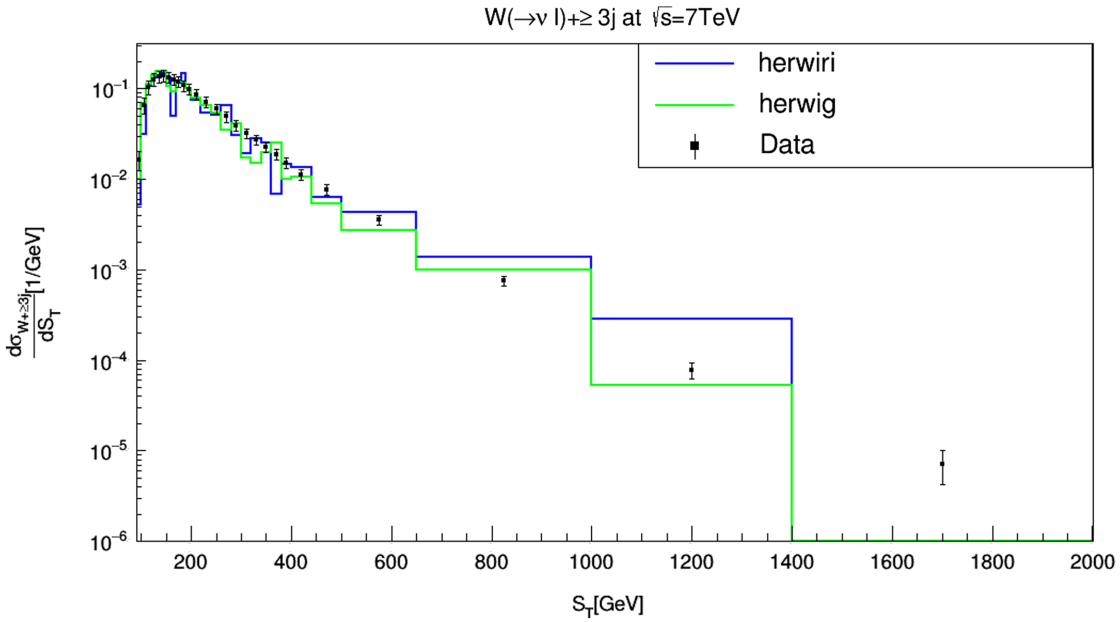

FIG. 23. Cross section for the production of $W+$jets as a function of the scalar sum S_T in $N_{\text{jet}} \geq 3$. The data are compared to predictions from MADGRAPH5_aMC@NLO/HERWIRI1.031 and MADGRAPH5_aMC@NLO/HERWIG6.521.

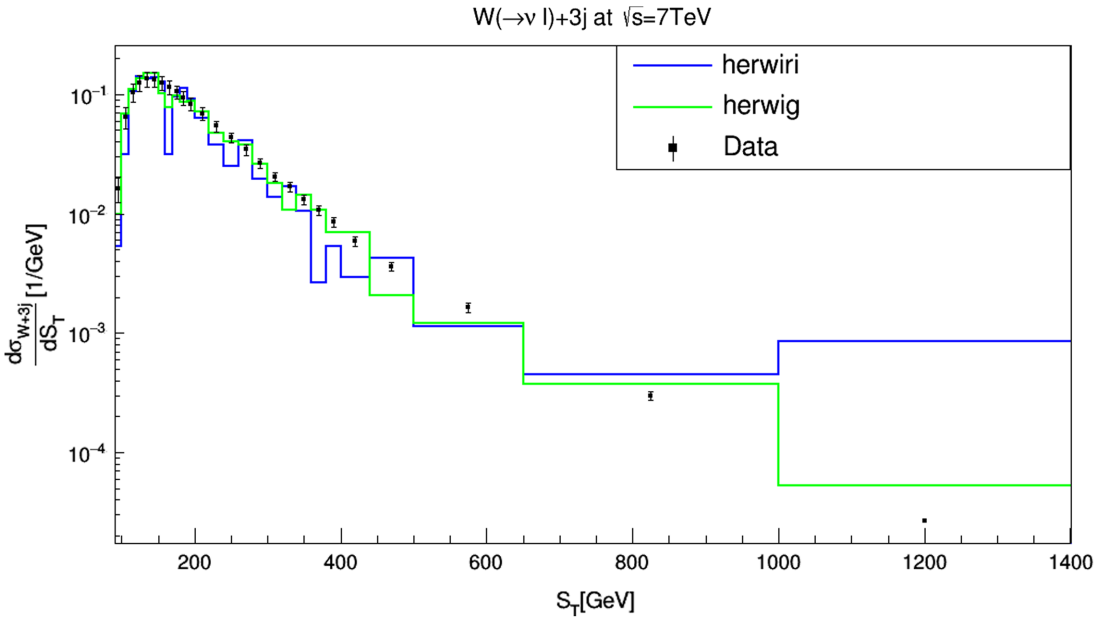

FIG. 24. Cross section for the production of $W+$jets as a function of the scalar sum S_T in $N_{\text{jet}} = 3$. The data are compared to predictions from MADGRAPH5_aMC@NLO/HERWIRI1.031 and MADGRAPH5_aMC@NLO/HERWIG6.521.

data. For large S_T values, in some cases HERWIG gives a better fit to the data.

The differential cross sections for the production of $W+2$ jets as a function of the scalar sum S_T are shown in Fig. 22. Good agreement is provided by the predictions of HERWIG for $S_T < 200$ GeV, where $(\frac{\chi^2}{\text{d.o.f}})_{\text{HERWIRI}} = 4.39$ and $(\frac{\chi^2}{\text{d.o.f}})_{\text{HERWIRI}} = 5.27$. HERWIRI in general gives either a better fit to the data or less discrepancy in comparison with HERWIG.

The differential cross sections for the production of $W+\geq 3$ jets as a function of the scalar sum S_T are shown in Fig. 23. For $S_T < 200$ GeV, the predictions provided by HERWIG give a better fit to the data where $(\frac{\chi^2}{\text{d.o.f}})_{\text{HERWIRI}} = 3.80$ and $(\frac{\chi^2}{\text{d.o.f}})_{\text{HERWIRI}} = 1.05$.

The differential cross sections for the production of $W+3$ jets as a function of the scalar sum S_T are shown in Fig. 24. For $S_T < 200$ GeV, the predictions provided by HERWIG give a better fit to the data, with $(\frac{\chi^2}{\text{d.o.f}})_{\text{HERWIRI}} = 4.54$ and $(\frac{\chi^2}{\text{d.o.f}})_{\text{HERWIRI}} = 1.30$.

It is clear in some cases HERWIRI predictions are in agreement with the data and in some cases HERWIG predictions give a better fit to the data. In general, a better agreement is provided for the lower jet multiplicities, e.g., $W+1$ jet and $W+\geq 1$ jet.

F. Cross sections

The cross sections for $W \to l + \nu_l$ production as functions of the inclusive and exclusive jet multiplicity are shown in Figs. 25 and 26. Figure 25 shows the cross sections for the production of $W+$ jet as a function of the

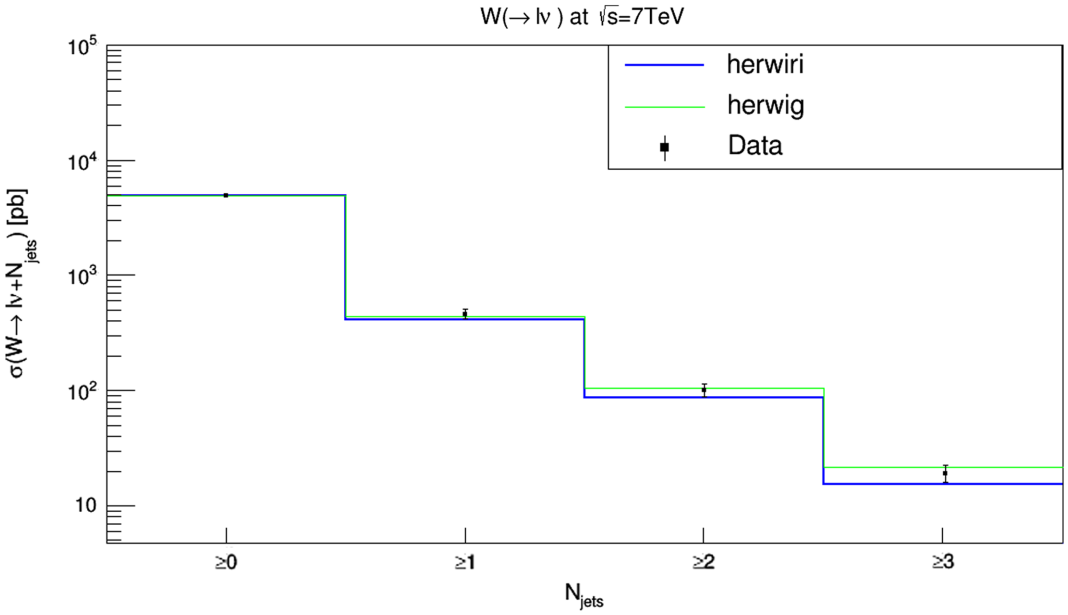

FIG. 25. Cross section for the production of $W+$ jets as a function of the inclusive jet multiplicity. The data are compared to predictions from MADGRAPH5_aMC@NLO/HERWIRI1.031 and MADGRAPH5_aMC@NLO/HERWIG6.521.

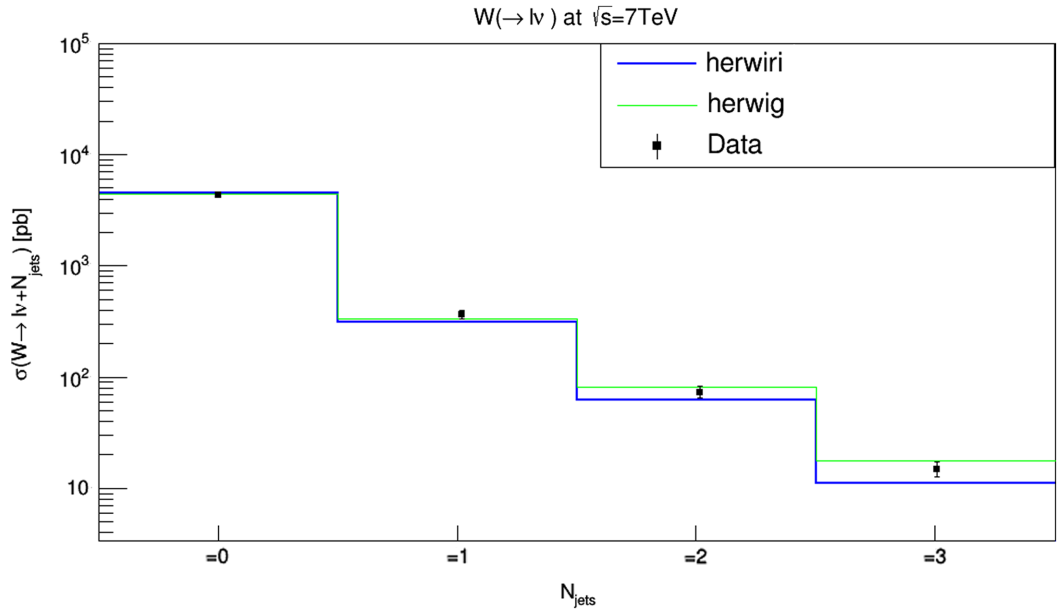

FIG. 26. Cross section for the production of $W+$ jets as a function of the exclusive jet multiplicity. The data are compared to predictions from MADGRAPH5_aMC@NLO/HERWIRI1.031 and MADGRAPH5_aMC@NLO/HERWIG6.521.

inclusive jet multiplicity. A good fit is provided by HERWIRI and HERWIG for $N_{\rm jet} \geq 1$, for $N_{\rm jet} \geq 2$, and for $N_{\rm jet} \geq 3$, where the HERWIRI prediction is just at the edge of the lower error bar on the data. For the exclusive case in Fig. 26, similar comments apply except that for the $N_{\rm jet} = 3$ case the HERWIRI prediction is about 2σ below the data.

V. RESULTS (CMS COLLABORATION)

In this section the measured $W(\to \mu + \nu_\mu) +$ jets fiducial cross sections [40] are shown and compared to the predictions of MADGRAPH5_aMC@NLO/HERWIRI1.031 and MADGRAPH5_aMC@NLO/HERWIG6.521, which are hereafter oftentimes referred to as HERWIRI and HERWIG, respectively. Each distribution is combined separately by minimizing a χ^2 function. The factors applied to the theory predictions are summarized in Appendix B.

A. Transverse momentum distributions P_T

The differential cross sections in jet P_T for inclusive jet multiplicities from 1 to 3 are shown in Figs. 27–29, and compared with predictions provided by HERWIRI and HERWIG. The differential cross sections as functions of the first three leading jets are shown in Figs. 27, 28, and 29. In Fig. 27, for $P_T < 150$ GeV, the predictions provided by HERWIRI and HERWIG give a very good fit to the data, with $(\frac{\chi^2}{\rm d.o.f})_{\rm HERWIRI} = 0.64$ and $(\frac{\chi^2}{\rm d.o.f})_{\rm HERWIRI} = 0.35$.

In Fig. 28, for $P_T < 110$ GeV, a better fit is provided by HERWIG to the data points, where $(\frac{\chi^2}{\rm d.o.f})_{\rm HERWIRI} = 1.43$ and $(\frac{\chi^2}{\rm d.o.f})_{\rm HERWIRI} = 0.73$. For higher values of P_T, the predictions provided by HERWIRI lie below the data while the HERWIG results either underestimate or overestimate the data.

In Fig. 29, for $P_T < 150$ GeV, the HERWIG predictions, in general, give a better fit to the data: $(\frac{\chi^2}{\rm d.o.f})_{\rm HERWIRI} = 2.60$ and $(\frac{\chi^2}{\rm d.o.f})_{\rm HERWIRI} = 1.59$.

B. The scalar sum of jet transverse momenta H_T

In this subsection, the differential cross sections are shown as functions of H_T for inclusive jet multiplicities 1–3. The scalar sum H_T is defined as

$$H_T = \sum_{i=1}^{N_{\rm jet}} P_T(j_i) \tag{21}$$

for each event.

The differential cross sections as a function of H_T for inclusive jet multiplicities 1–3 are shown in Figs. 30–32. In Fig. 30, for $H_T < 300$ GeV, the predictions provided by HERWIRI and HERWIG give a very good fit to the data with $(\frac{\chi^2}{\rm d.o.f})_{\rm HERWIRI} = 0.57$ and $(\frac{\chi^2}{\rm d.o.f})_{\rm HERWIRI} = 0.40$. In Fig. 31, for $H_T < 180$ GeV and $360 < H_T < 540$ GeV, HERWIRI gives a better fit to the data while in Fig. 32 the predictions provided by HERWIRI give a better fit to the data for $H_T < 250$ GeV. In Fig. 31, for $H_T < 300$ GeV, $(\frac{\chi^2}{\rm d.o.f})_{\rm HERWIRI} = 1.70$ and $(\frac{\chi^2}{\rm d.o.f})_{\rm HERWIRI} = 1.36$. In Fig. 32, for $H_T < 250$ GeV $(\frac{\chi^2}{\rm d.o.f})_{\rm HERWIRI} = 4.02$ and $(\frac{\chi^2}{\rm d.o.f})_{\rm HERWIRI} = 4.37$.

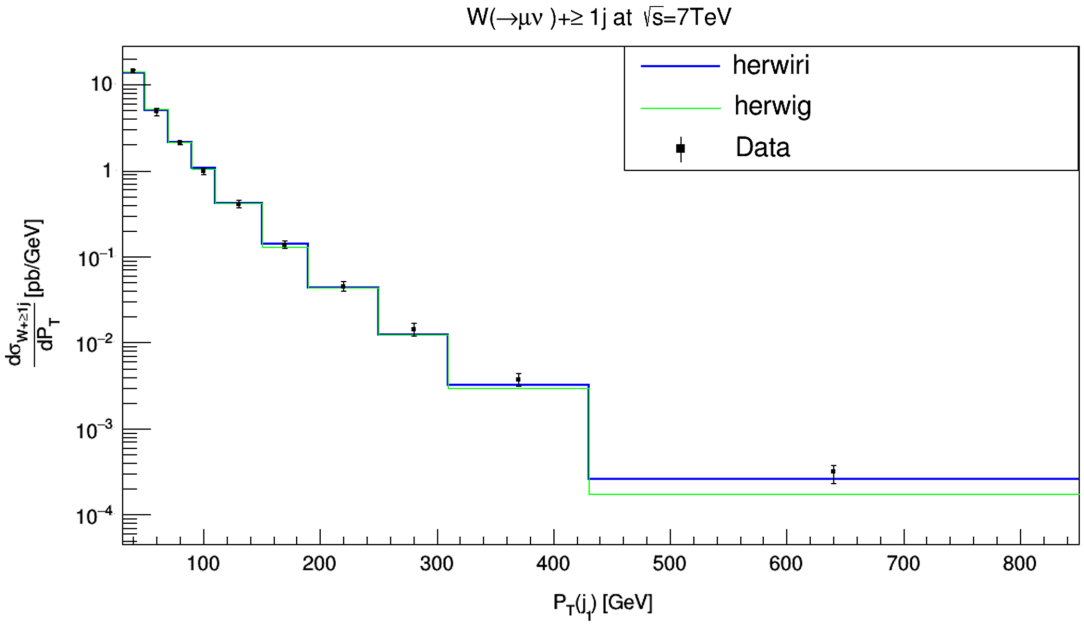

FIG. 27. Cross section for the production of $W +$ jets as a function of the leading jet P_T for $N_{\rm jet} \geq 1$. The data are compared to predictions from MADGRAPH5_aMC@NLO/HERWIRI1.031 and MADGRAPH5_aMC@NLO/HERWIG6.521.

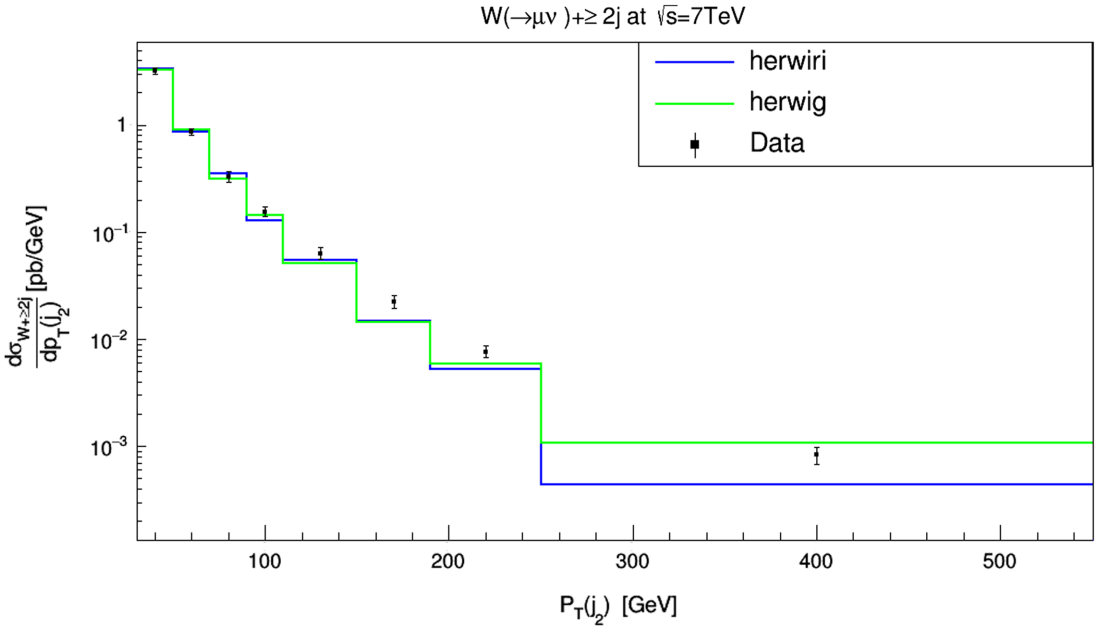

FIG. 28. Cross section for the production of W + jets as a function of the second leading jet P_T for $N_{\text{jet}} \geq 2$. The data are compared to predictions from MADGRAPH5_aMC@NLO/HERWIRI1.031 and MADGRAPH5_aMC@NLO/HERWIG6.521.

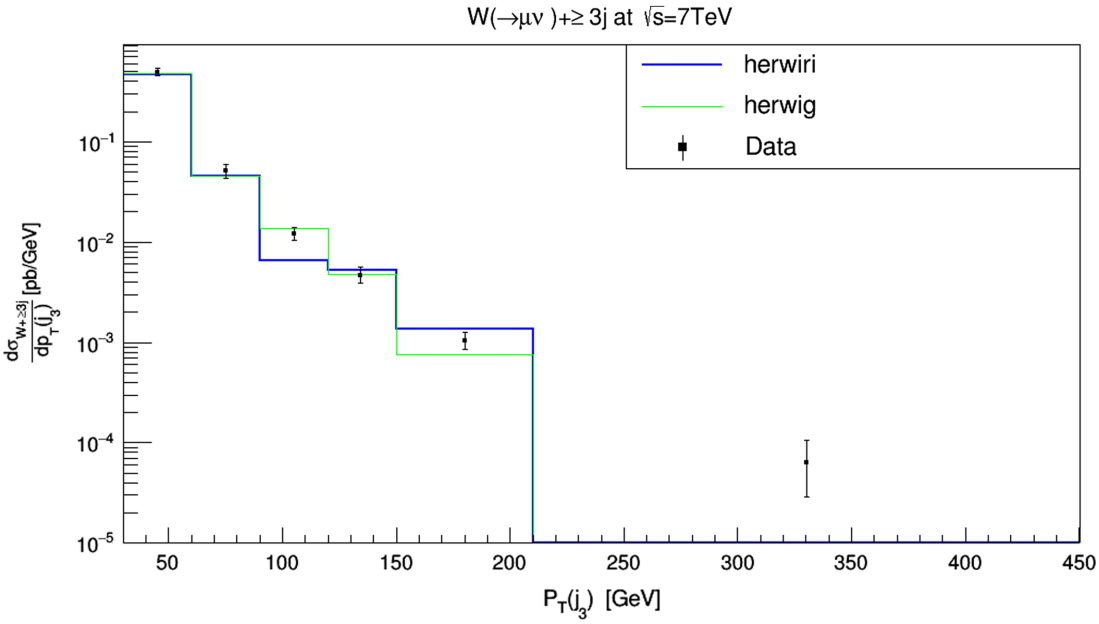

FIG. 29. Cross section for the production of W + jets as a function of the third leading jet P_T for $N_{\text{jet}} \geq 3$. The data are compared to predictions from MADGRAPH5_aMC@NLO/HERWIRI1.031 and MADGRAPH5_aMC@NLO/HERWIG6.521.

C. Pseudorapidity distributions $|\eta(j)|$

In this section, the differential cross sections are shown as functions of pseudorapidities of the three leading jets. The pseudorapidity, which was defined in Eq. (12), can be written as

$$\eta = \frac{1}{2}\ln\left(\frac{|\vec{P}| + P_L}{|\vec{P}| - P_L}\right) = \text{arctan}h\left(\frac{P_L}{|\vec{P}|}\right), \tag{22}$$

where P_L is the component of the momentum along the beam axis.

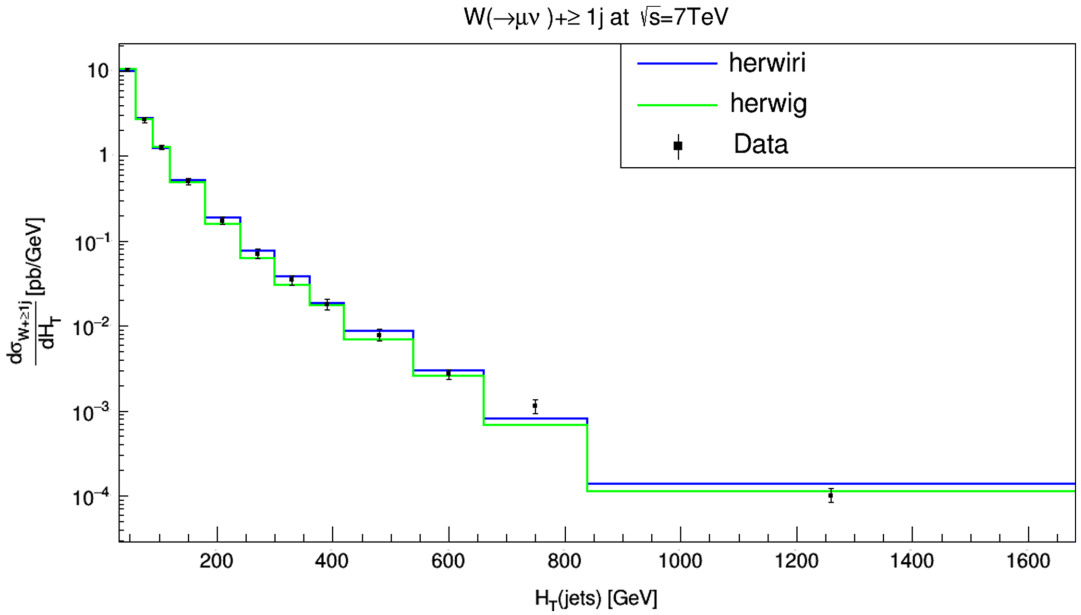

FIG. 30. Cross section for the production of $W+$jets as a function of H_T for $N_{\text{jet}} \geq 1$. The data are compared to predictions from MADGRAPH5_aMC@NLO/HERWIRI1.031 and MADGRAPH5_aMC@NLO/HERWIG6.521.

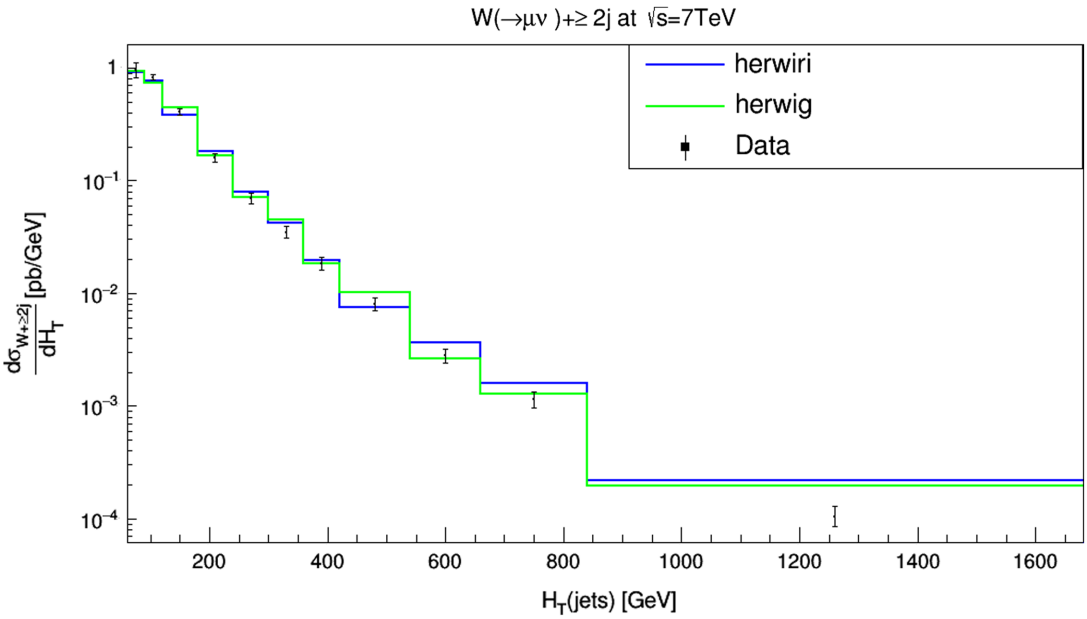

FIG. 31. Cross section for the production of $W+$jets as a function of H_T for $N_{\text{jet}} \geq 2$. The data are compared to predictions from MADGRAPH5_aMC@NLO/HERWIRI1.031 and MADGRAPH5_aMC@NLO/HERWIG6.521.

The problem with rapidity is that it can be hard to measure for highly relativistic particles. We need the total momentum vector of a particle, especially at high values of the rapidity where the z component of the momentum is large, and the beam pipe can be in the way of measuring it precisely.

However, there is a way of defining a quantity that is almost the same thing as the rapidity which is much easier to measure than y for highly energetic particles. This leads to the concept of the pseudorapidity η, wherein we see from Eq. (22) that the magnitude of the momentum cancels out of the ratio in the arguments of the logarithm and the arctanh in the equation.

Hadron colliders measure physical momenta in terms of transverse momentum, P_T, polar angle in the transverse plane, ϕ, and pseudorapidity. To obtain Cartesian momenta

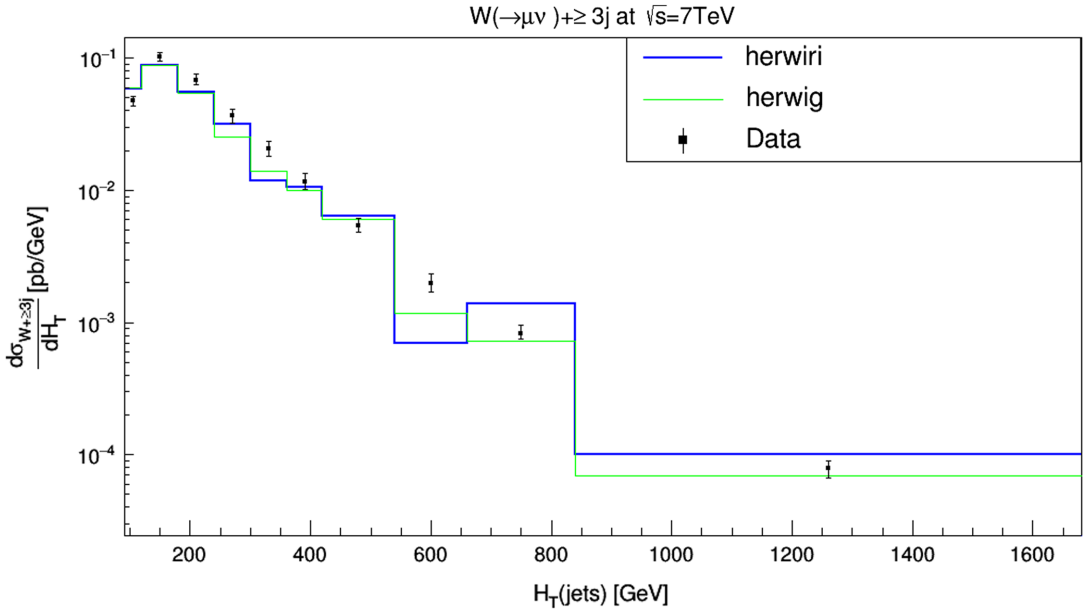

FIG. 32. Cross section for the production of $W+$jets as a function of H_T for $N_{\text{jet}} \geq 3$. The data are compared to predictions from MADGRAPH5_aMC@NLO/HERWIRI1.031 and MADGRAPH5_aMC@NLO/HERWIG6.521.

(P_x, P_y, P_z) (with the z axis defined as the beam axis), the following conversions are used:

$$\begin{cases} P_x = P_T \cos\phi, \\ P_y = P_T \sin\phi, \\ P_z = P_T \sinh\eta. \end{cases} \tag{23}$$

In Fig. 33 the cross section is shown as a function of $|\eta(j_1)|$, the leading jet pseudorapidity. The predictions provided by HERWIRI and HERWIG are in good agreement with the data, with $(\frac{\chi^2}{\text{d.o.f}})_{\text{HERWIRI}} = 0.39$ and $(\frac{\chi^2}{\text{d.o.f}})_{\text{HERWIRI}} = 0.79$. In Fig. 34, in general, HERWIG gives a better fit to the data, with $(\frac{\chi^2}{\text{d.o.f}})_{\text{HERWIRI}} = 1.94$ and $(\frac{\chi^2}{\text{d.o.f}})_{\text{HERWIRI}} = 1.71$. Figure 35 shows that HERWIRI

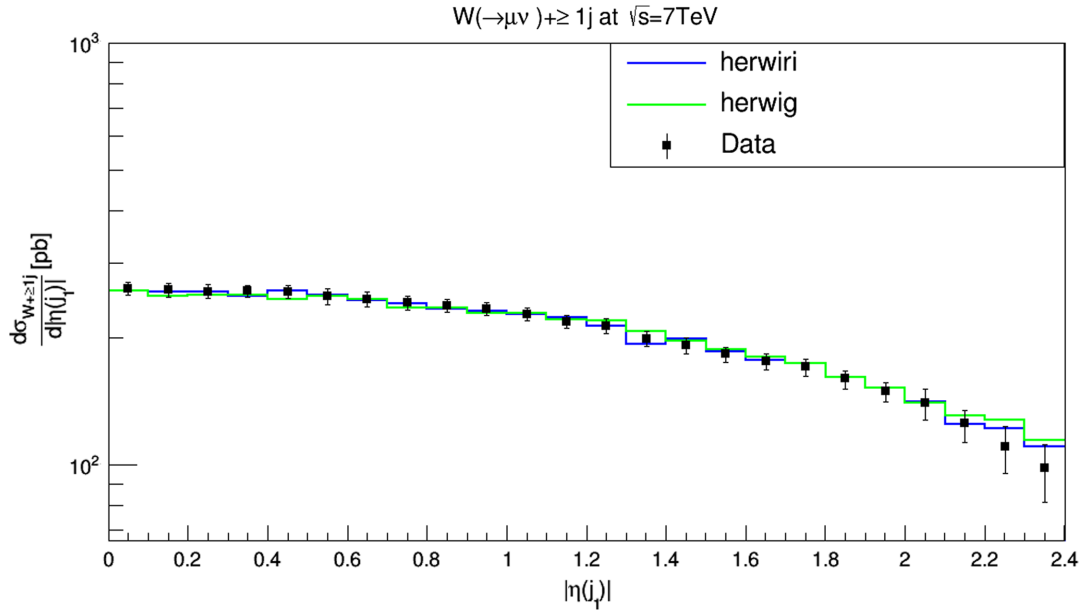

FIG. 33. Cross section for the production of $W+$jets as a function of $|\eta(j_1)|$ for $N_{\text{jet}} \geq 1$. The data are compared to predictions from MADGRAPH5_aMC@NLO/HERWIRI1.031 and MADGRAPH5_aMC@NLO/HERWIG6.521.

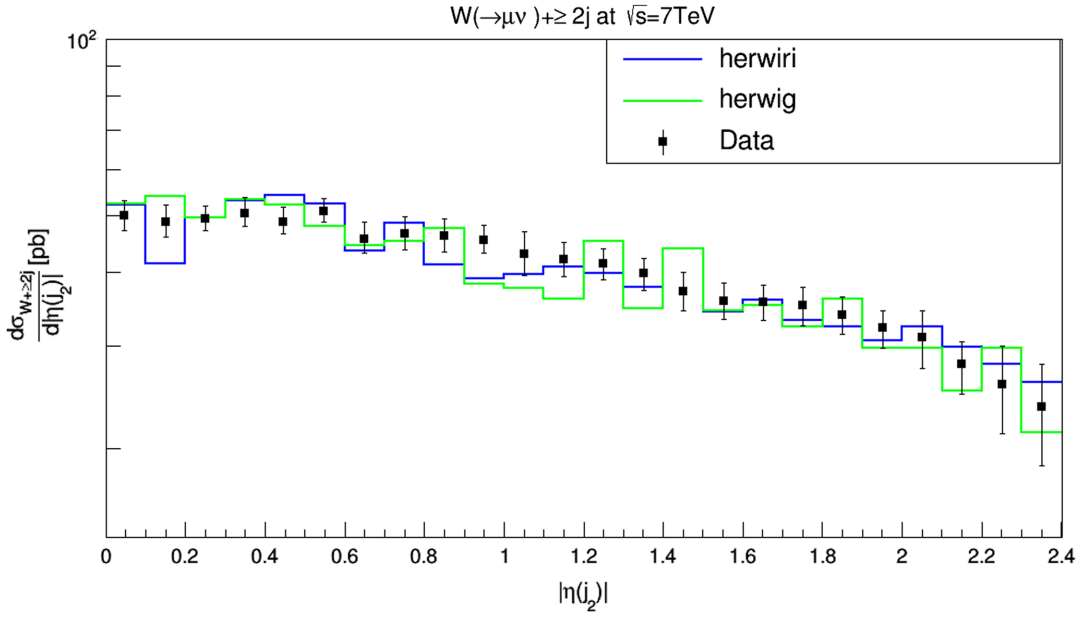

FIG. 34. Cross section for the production of $W+$ jets as a function of $|\eta(j_2)|$ for $N_{\text{jet}} \geq 2$. The data are compared to predictions from MADGRAPH5_aMC@NLO/HERWIRI1.031 and MADGRAPH5_aMC@NLO/HERWIG6.521.

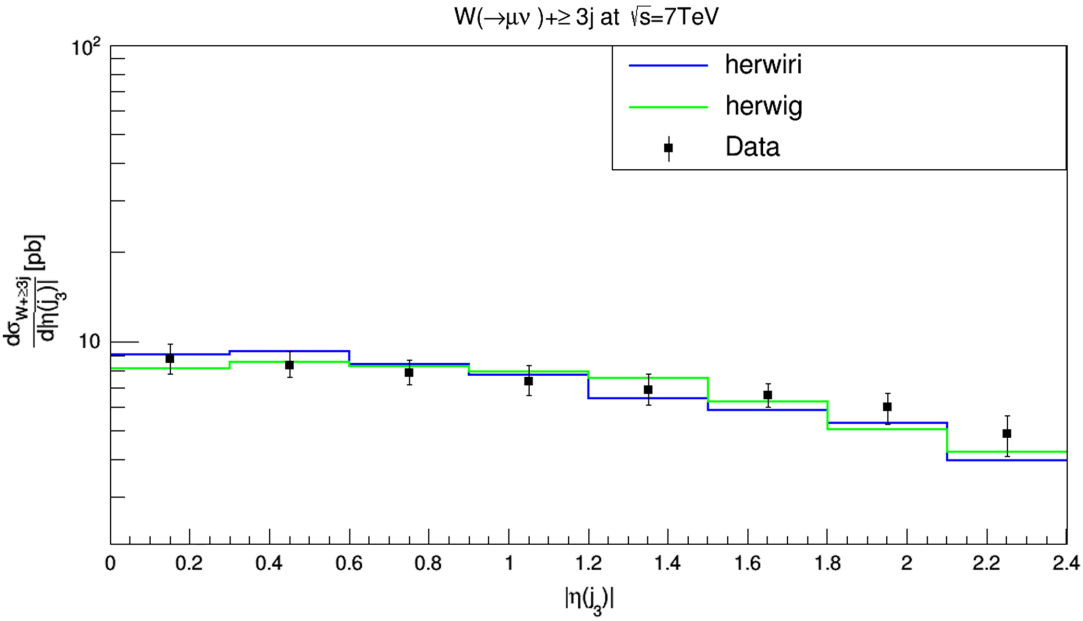

FIG. 35. Cross section for the production of $W+$ jets as a function of $|\eta(j_1)|$ for $N_{\text{jet}} \geq 3$. The data are compared to predictions from MADGRAPH5_aMC@NLO/HERWIRI1.031 and MADGRAPH5_aMC@NLO/HERWIG6.521.

and HERWIG predictions are in agreement with the data, with $(\frac{\chi^2}{\text{d.o.f}})_{\text{HERWIRI}} = 0.82$ and $(\frac{\chi^2}{\text{d.o.f}})_{\text{HERWIRI}} = 0.61$.

D. Azimuthal angular distribution between the muon and the leading jet

The differential cross sections are shown as functions of the azimuthal angle between the muon and the first three leading jets for inclusive jet multiplicities 1–3. The azimuthal angle between the muon and the leading jet is defined as

$$\cos(\Delta\Phi(\mu, j_1)) = \frac{P_x(\mu)P_x(j_1) + P_y(\mu)P_y(j_1)}{\sqrt{P_x^2(\mu) + P_y^2(\mu)}\sqrt{P_x^2(j_1) + P_y^2(j_1)}}, \tag{24}$$

with

$$\begin{cases} \mu^{\mu} = (E_{\mu}, P_x(\mu), P_y(\mu), P_L(\mu)), \\ j_1^{\mu} = (E_{j_1}, P_x(j_1), P_y(j_1), P_L(j_1)). \end{cases} \tag{25}$$

The differential cross sections as functions of the azimuthal angle between the muon and the first three leading jets are shown in Figs. 36–38 for inclusive jet multiplicities 1–3, respectively.

In Fig. 36, the data are better modeled by the predictions provided by HERWIRI as expected. Figure 37 shows that the HERWIG predictions give a better fit to the data. In Fig. 38, the predictions provided by either HERWIRI and HERWIG are in good agreement with the data. In Fig. 36, $(\frac{\chi^2}{\text{d.o.f}})_{\text{HERWIRI}} = 1.26$ and $(\frac{\chi^2}{\text{d.o.f}})_{\text{HERWIRI}} = 2.67$. In Fig. 37,

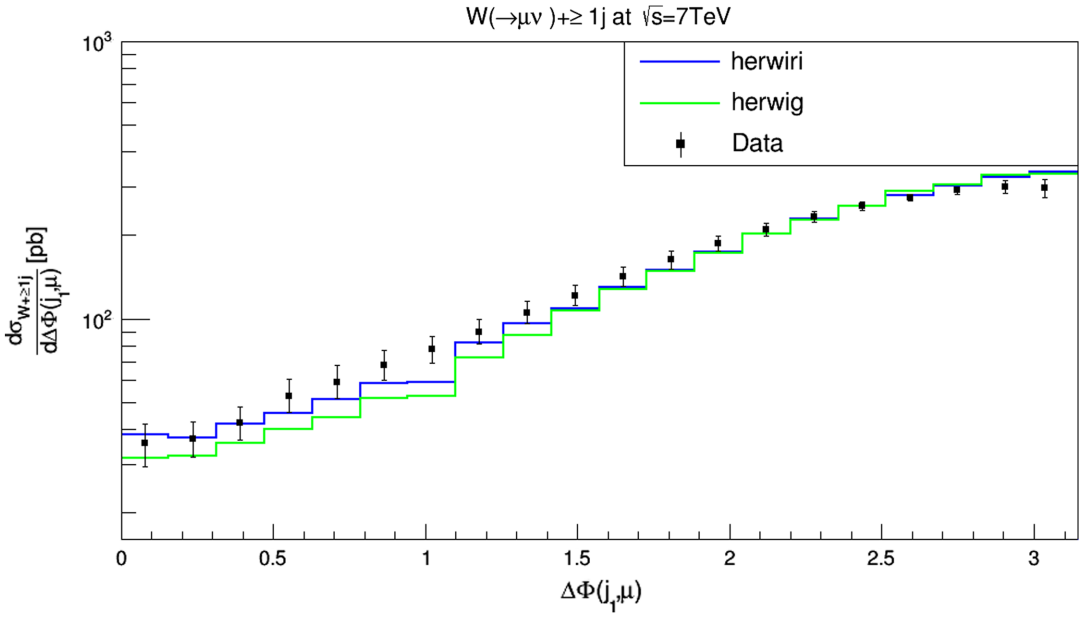

FIG. 36. Cross section for the production of $W+$jets as a function of the azimuthal angle between the muon and the leading jet $\Delta\Phi(\mu, j_1)$ for $N_{\text{jet}} \geq 1$. The data are compared to predictions from MADGRAPH5_aMC@NLO/HERWIRI1.031 and MADGRAPH5_aMC@NLO/HERWIG6.521.

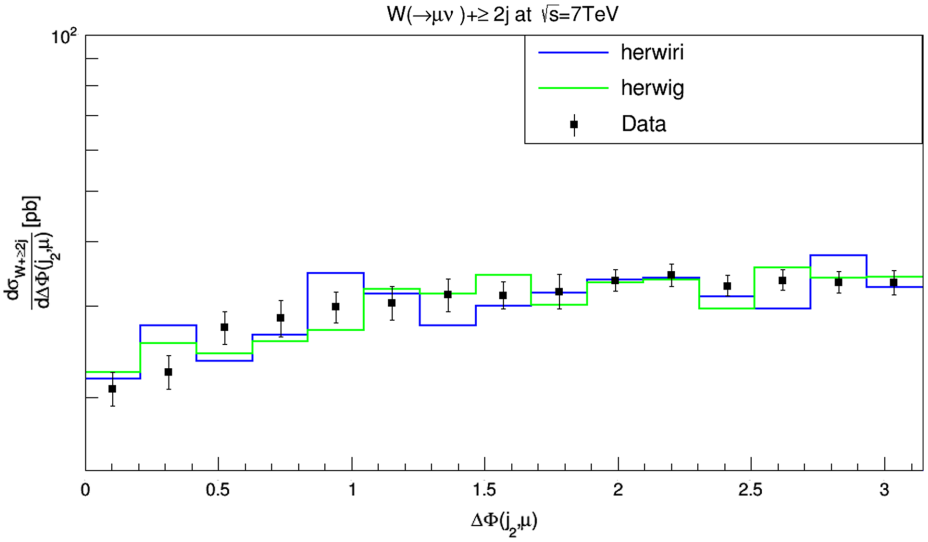

FIG. 37. Cross section for the production of $W+$jets as a function of the azimuthal angle between the muon and the second leading jet $\Delta\Phi(\mu, j_2)$ for $N_{\text{jet}} \geq 2$. The data are compared to predictions from MADGRAPH5_aMC@NLO/HERWIRI1.031 and MADGRAPH5_aMC@NLO/HERWIG6.521.

$(\frac{\chi^2}{\text{d.o.f}})_{\text{HERWIRI}} = 2.73$ and $(\frac{\chi^2}{\text{d.o.f}})_{\text{HERWIRI}} = 1.48$. In Fig. 38, $(\frac{\chi^2}{\text{d.o.f}})_{\text{HERWIRI}} = 0.89$ and $(\frac{\chi^2}{\text{d.o.f}})_{\text{HERWIRI}} = 0.61$.

E. Cross sections

The measured $W(\to\mu+\nu_\mu)+\text{jets}$ fiducial cross sections are shown in Figs. 39 and 40 and compared to the predictions of MADGRAPH5_aMC@NLO/HERWIRI1.031 and MADGRAPH5_aMC@NLO/HERWIG6.521. Figure 39 shows the differential cross sections for the inclusive jet multiplicities 1–3. HERWIRI gives a better fit to the data. Figure 40 shows the differential cross sections for the exclusive jet multiplicities 1–3. The cross sections provided by HERWIG give a better fit to the data. In Fig. 39, $(\frac{\chi^2}{\text{d.o.f}})_{\text{HERWIRI}} = 0.46$ and $(\frac{\chi^2}{\text{d.o.f}})_{\text{HERWIRI}} = 0.56$ while in Fig. 40, $(\frac{\chi^2}{\text{d.o.f}})_{\text{HERWIRI}} = 1.16$ and $(\frac{\chi^2}{\text{d.o.f}})_{\text{HERWIRI}} = 0.83$.

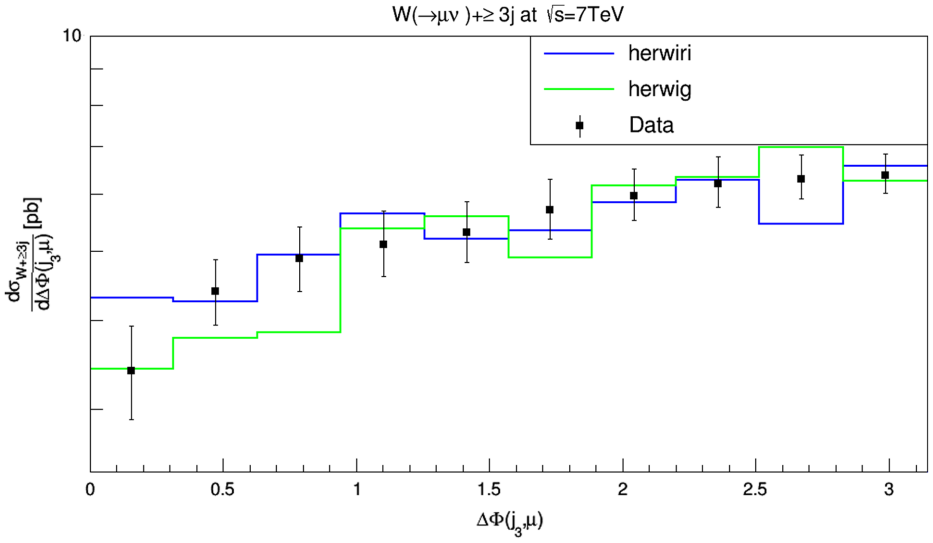

FIG. 38. Cross section for the production of $W+\text{jets}$ as a function of the azimuthal angle between the muon and the second leading jet $\Delta\Phi(\mu, j_3)$ for $N_{\text{jet}} \geq 3$. The data are compared to predictions from MADGRAPH5_aMC@NLO/HERWIRI1.031 and MADGRAPH5_aMC@NLO/HERWIG6.521.

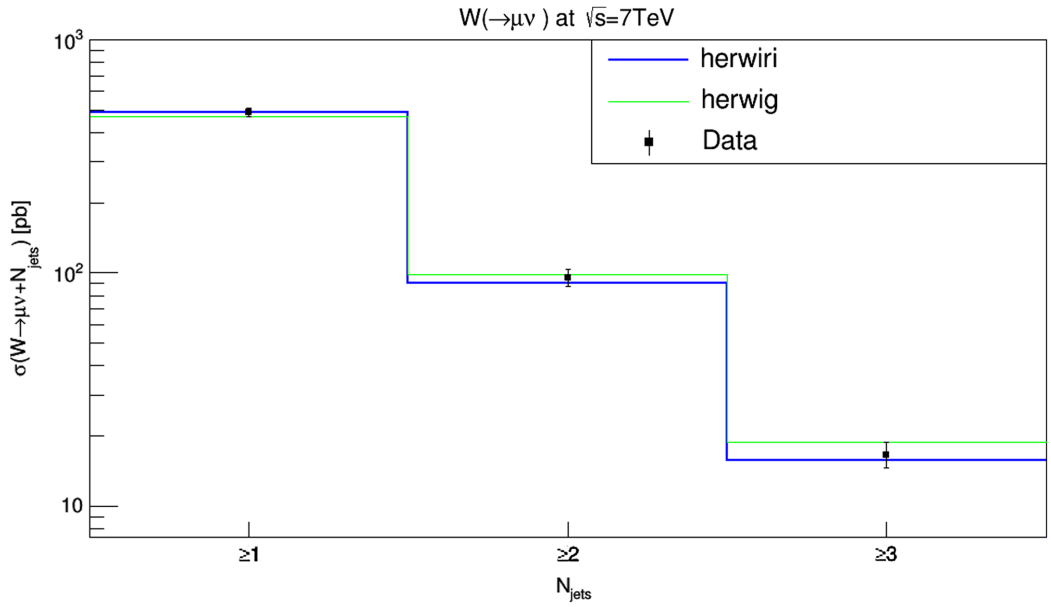

FIG. 39. Measured cross section versus inclusive jet multiplicity. The data are compared to predictions from MADGRAPH5_aMC@NLO/HERWIRI1.031 and MADGRAPH5_aMC@NLO/HERWIG6.521.

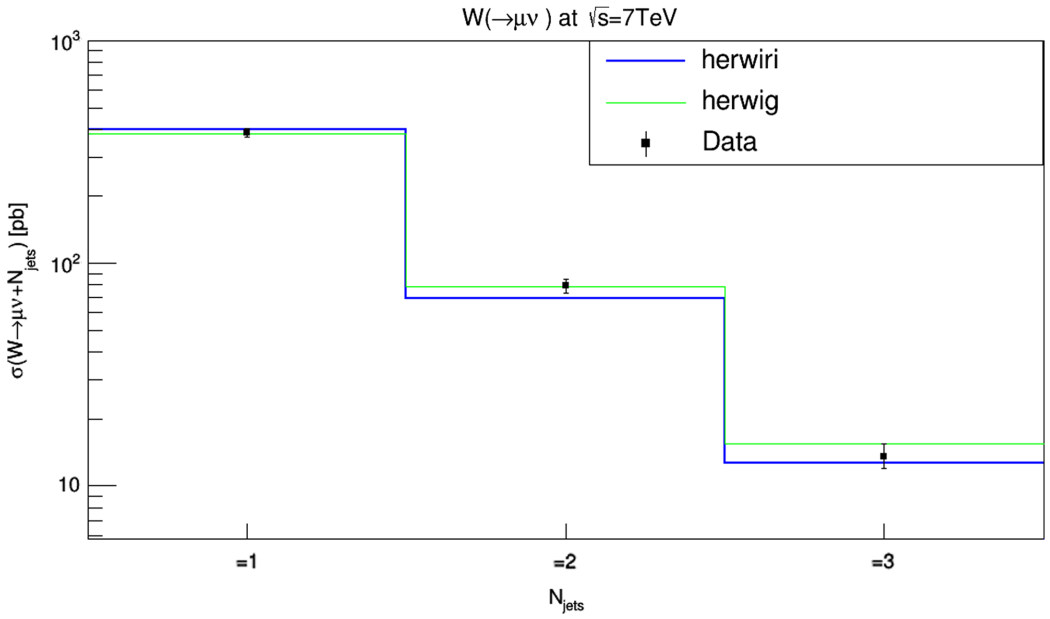

FIG. 40. Measured cross section versus exclusive jet multiplicity. The data are compared to predictions from MADGRAPH5_aMC@NLO/HERWIRI1.031 and MADGRAPH5_aMC@NLO/HERWIG6.521.

VI. THEORETICAL PREDICTIONS AND ASSOCIATED ERRORS

Madgraph_aMC@NLO is only capable of doing the leading-order (LO) and next-to-leading order (NLO) calculations. That being said, the theoretical predictions provided by Madgraph_aMC@NLO would have theoretical errors around 15%–20%. For the sake of clarification, four sample plots are given in Appendix D (see Figs. 49–52). In the process of generating these sample plots, 20% of the theoretical error has been taken into account.

VII. SUMMARY

The realization of the IR-improved DGLAP-CS theory, when used in the MADGRAPH5_aMC@NLO/HERWIRI1.031 $\mathcal{O}(\alpha)$ matrix element-matched parton shower framework, provides us with the opportunity to explain, in the soft regime, the differential cross sections for a W boson produced in association with jets in pp collisions in the recent LHC data from ATLAS and CMS, without the need of an unexpectedly hard intrinsic Gaussian distribution with an rms value of PTRMS $=$ 2.2 GeV in parton's wave function. PTRMS is the rms value of the intrinsic Gaussian transverse momentum distribution for the partons inside the proton. In our view, this can be interpreted as providing a rigorous basis for the phenomenological correctness of such unexpectedly hard distributions insofar as describing these data using the usual unimproved DGLAP-CS showers is concerned.

APPENDIX A: SCALE FACTORS FOR THEORETICAL PREDICTIONS

TABLE III. Summary of the scale factors applied to the theoretical predictions for ATLAS at $\sqrt{s} = 7$ TeV. Note that the factor of 2 between the scalings of Figs. 1 and 7 is due to our having simulated for Y instead of the $|Y|$ in the data.

Figure number	$\alpha_{\mathrm{HERWIRI}}$	$\alpha_{\mathrm{HERWIRI}}$	$(\frac{\chi^2}{\mathrm{d.o.f}})_{\mathrm{HERWIRI}}$	$(\frac{\chi^2}{\mathrm{d.o.f}})_{\mathrm{HERWIRI}}$
Fig. 1	0.0201	0.02023	0.76	2.04
Fig. 2	0.0155	0.015	1.13	0.96
Fig. 3	0.03113	0.03241	1.19	1.49
Fig. 4	0.03501	0.03221	1.06	1.69
Fig. 5	0.01460	0.01481	0.27	0.20
Fig. 6	0.01562	0.01141	3.27	3.96
Fig. 7	0.03978	0.04038	0.35	0.71
Fig. 8	0.05890	0.06062	1.01	0.63
Fig. 9	0.02850	0.03601	1.05	0.43

(Table continued)

TABLE III. *(Continued)*

Figure number	α_{HERWIRI}	α_{HERWIRI}	$(\frac{\chi^2}{\text{d.o.f}})_{\text{HERWIRI}}$	$(\frac{\chi^2}{\text{d.o.f}})_{\text{HERWIRI}}$
Fig. 10	0.01311	0.0128	1.18	1.69
Fig. 11	0.08608	0.08051	2.08	4.77
Fig. 12	0.01311	0.01324	1.59	0.78
Fig. 13	0.01322	0.01328	1.46	0.49
Fig. 14	0.01980	0.01920	0.59	0.96
Fig. 15	0.01521	0.0139	2.50	0.76
Fig. 16	0.03116	0.03012	2.25	1.26
Fig. 17	0.03301	0.03178	2.36	1.09
Fig. 18	0.01476	0.01073	2.71	2.01
Fig. 19	0.01318	0.01231	3.73	0.80
Fig. 20	0.02013	0.02128	0.28	1.94
Fig. 21	0.03170	0.02913	2.96	1.65
Fig. 22	0.03212	0.03091	4.39	5.27
Fig. 23	0.01469	0.01108	3.80	1.05
Fig. 24	0.01350	0.01031	4.54	1.30
Fig. 25	0.5547	0.5309	4.31	0.70
Fig. 26	0.5420	0.5172	7.31	1.08

APPENDIX B: SCALE FACTORS FOR CMS AT $\sqrt{s} = 7$ TeV

TABLE IV. Summary of the scale factors applied to the theoretical predictions for CMS at $\sqrt{s} = 7$ TeV.

Figure number	α_{HERWIRI}	α_{HERWIRI}	$(\frac{\chi^2}{\text{d.o.f}})_{\text{HERWIRI}}$	$(\frac{\chi^2}{\text{d.o.f}})_{\text{HERWIRI}}$
Fig. 27	0.04373	0.04521	0.64	0.35
Fig. 28	0.0615	0.061	1.43	0.73
Fig. 29	0.52852	0.4025	2.60	1.59
Fig. 30	0.04382	0.0451	0.57	0.40
Fig. 31	0.06138	0.0599	1.70	1.36
Fig. 32	0.5261	0.390	4.02	4.37
Fig. 33	0.04635	0.046702	0.39	0.79
Fig. 34	0.06175	0.062021	1.94	1.71
Fig. 35	0.502	0.415	0.82	0.61
Fig. 36	0.0421	0.04411	1.26	2.67
Fig. 37	0.06011	0.05981	2.73	1.48
Fig. 38	0.5212	0.3978	0.89	0.61
Fig. 39	0.6836	0.559	0.46	0.56
Fig. 40	0.6251	0.5551	1.16	0.83

APPENDIX C: RATIO PLOTS

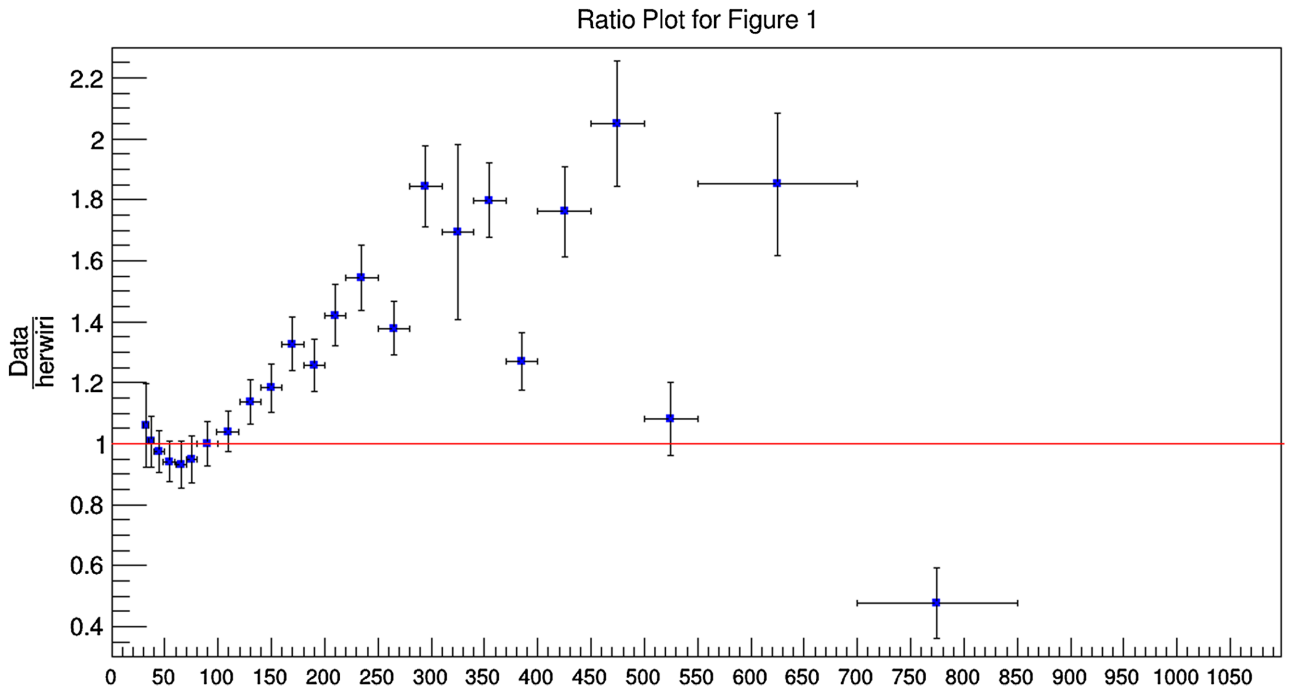

FIG. 41. Ratio plot for the production of W + jets as a function of the leading-jet P_T in $N_{\text{jet}} \geq 1$. The data are divided by predictions from MADGRAPH5_aMC@NLO/HERWIRI1.031.

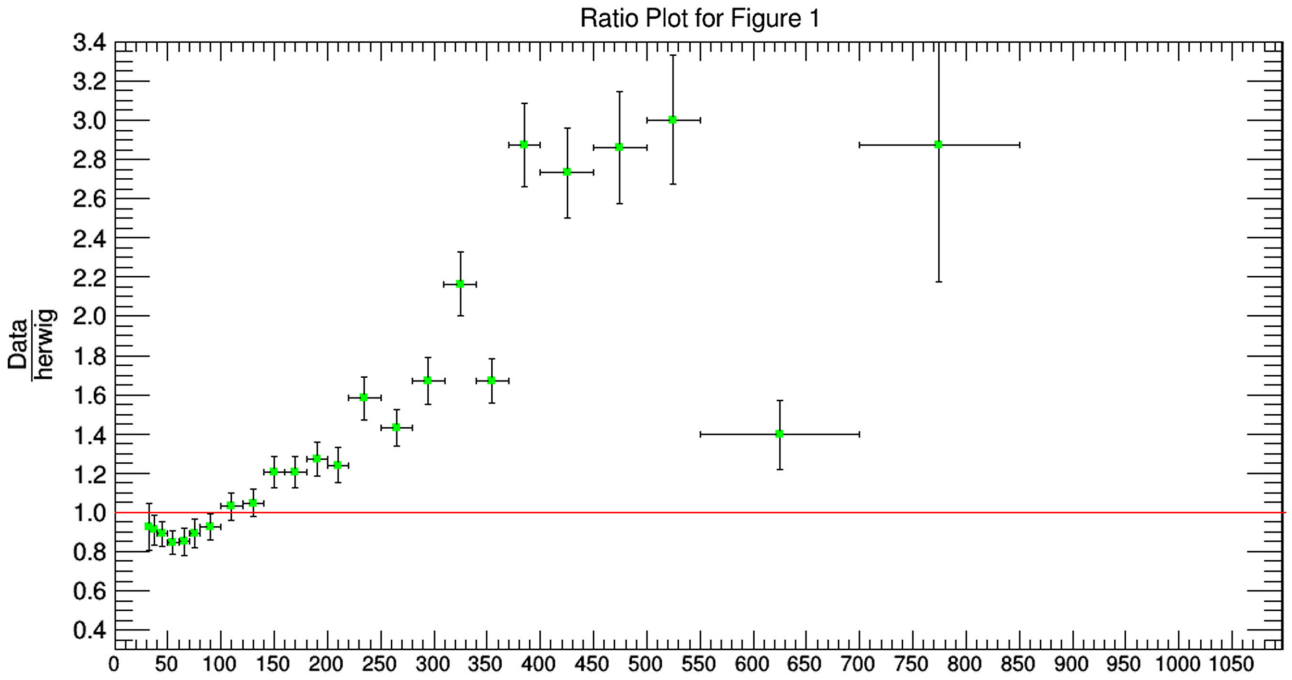

FIG. 42. Ratio plot for the production of $W +$ jets as a function of the leading-jet P_T in $N_{\text{jet}} \geq 1$. The data are divided by predictions from MADGRAPH5_aMC@NLO/HERWIG6.521.

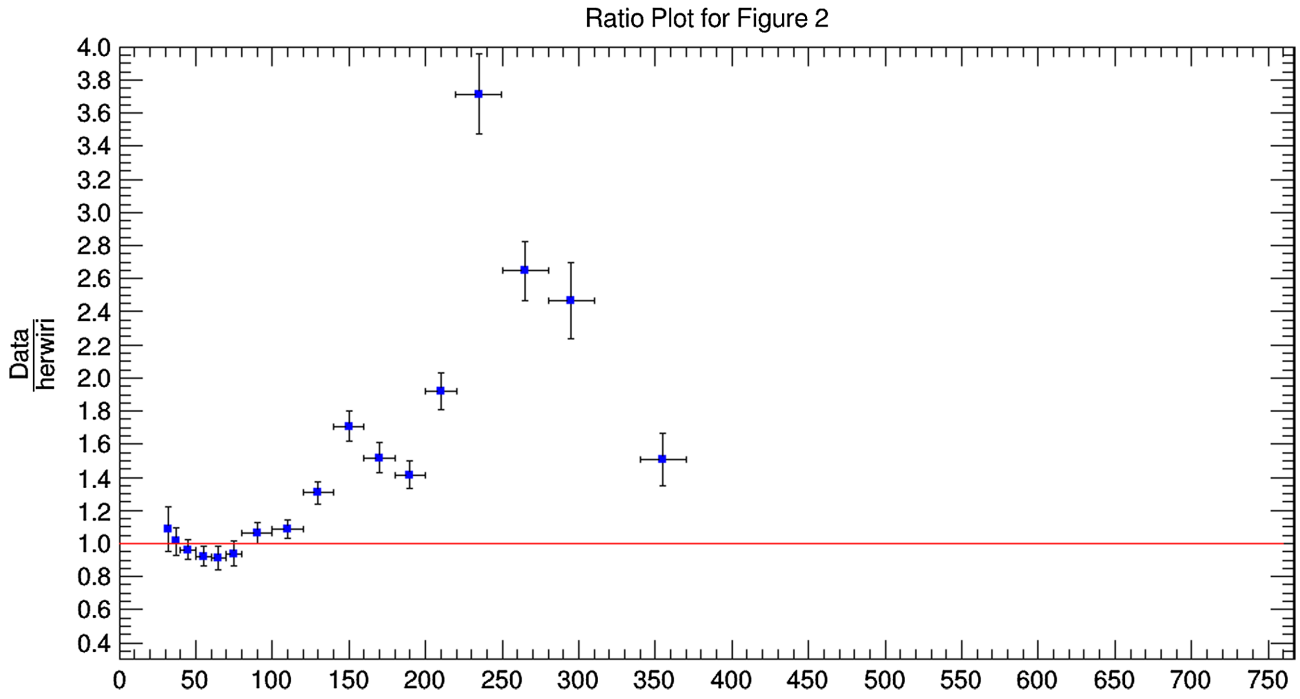

FIG. 43. Ratio plot for the production of $W +$ jets as a function of the leading-jet P_T in $N_{\text{jet}} = 1$. The data are divided by predictions from MADGRAPH5_aMC@NLO/HERWIRI1.031.

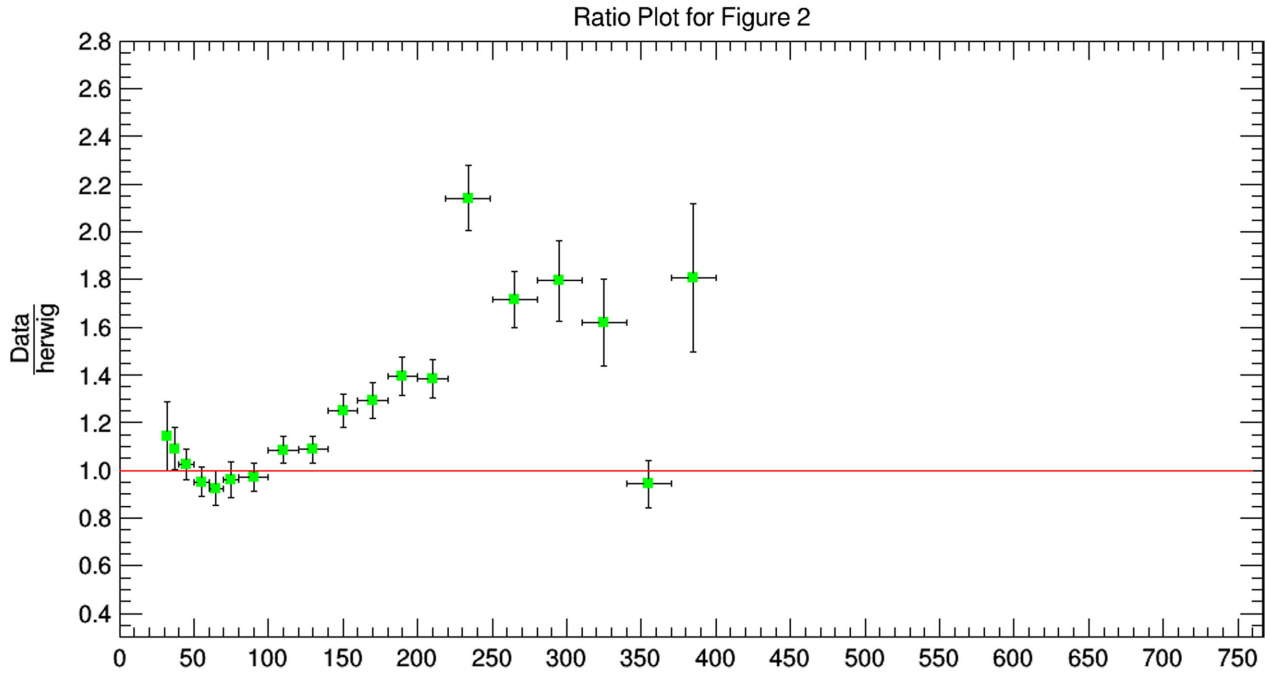

FIG. 44. Ratio plot for the production of $W+$ jets as a function of the leading-jet P_T in $N_{\text{jet}}=1$. The data are divided by predictions from MADGRAPH5_aMC@NLO/HERWIG6.521.

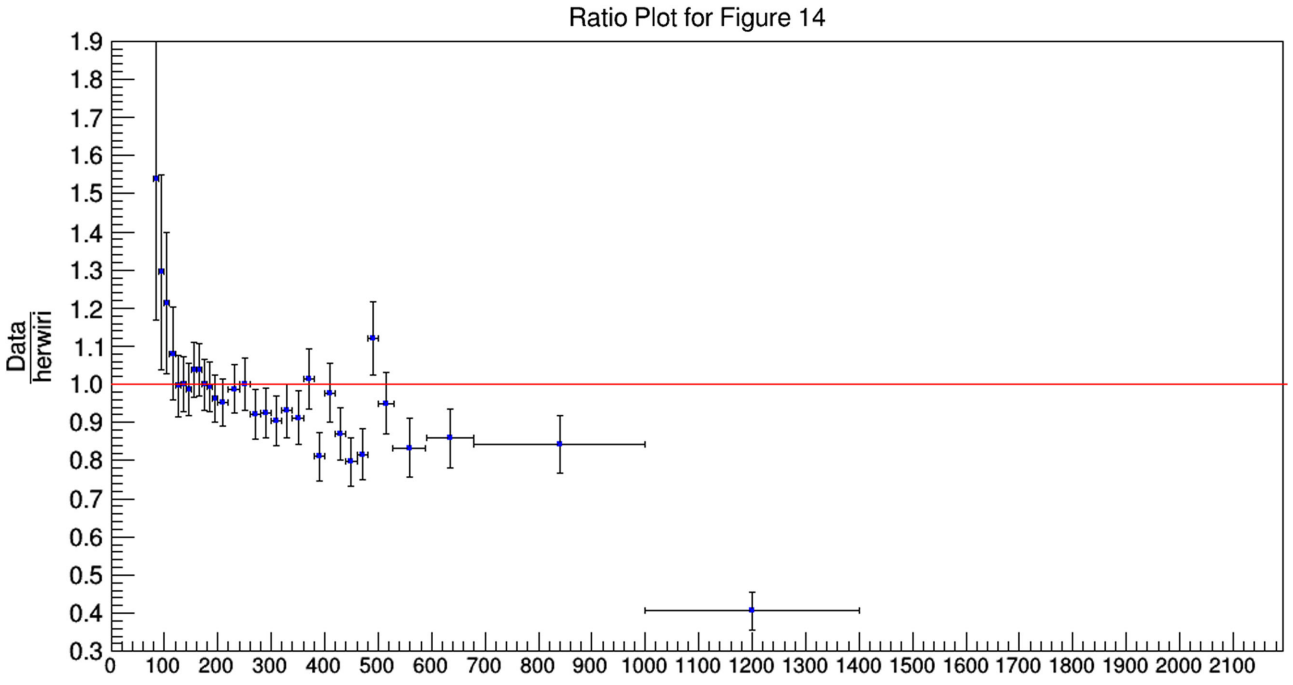

FIG. 45. Ratio plot for the production of $W+$ jets as a function of the scalar sum H_T in $N_{\text{jet}}\geq 1$. The data are divided by predictions from MADGRAPH5_aMC@NLO/HERWIRI1.031.

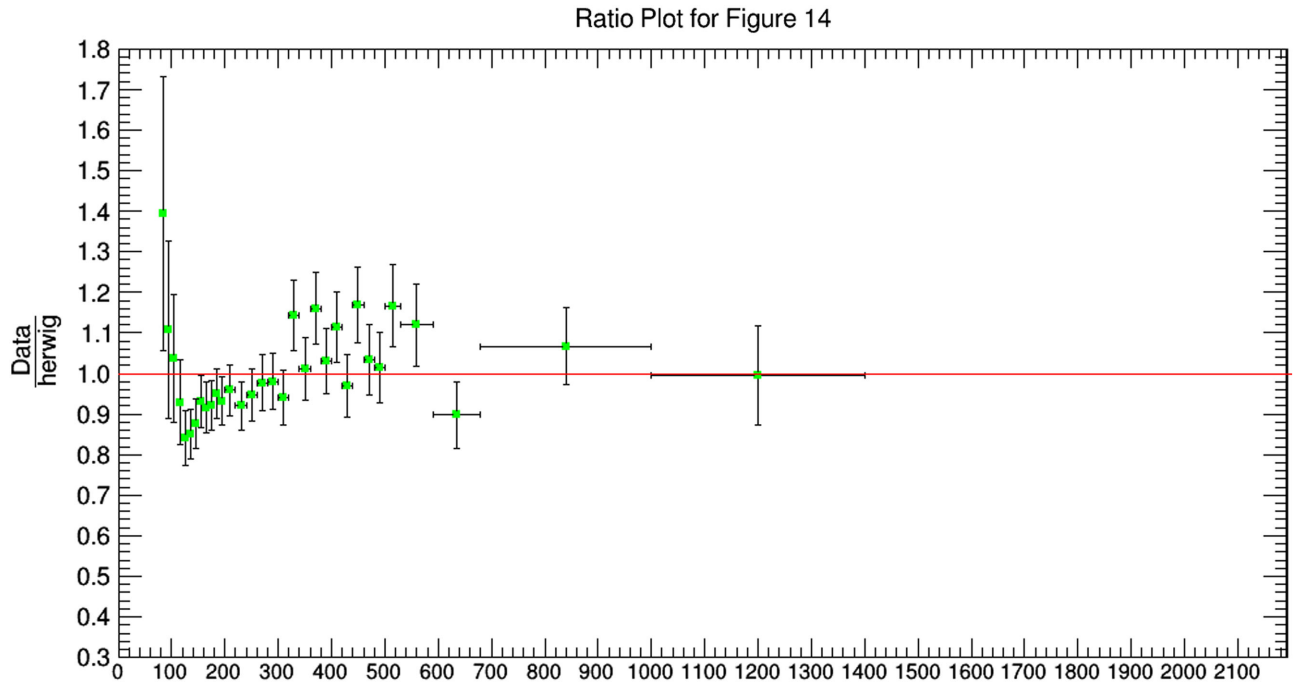

FIG. 46. Ratio plot for the production of $W +$ jets as a function of the scalar sum H_T in $N_{\text{jet}} \geq 1$. The data are divided by predictions from MADGRAPH5_aMC@NLO/HERWIG6.521.

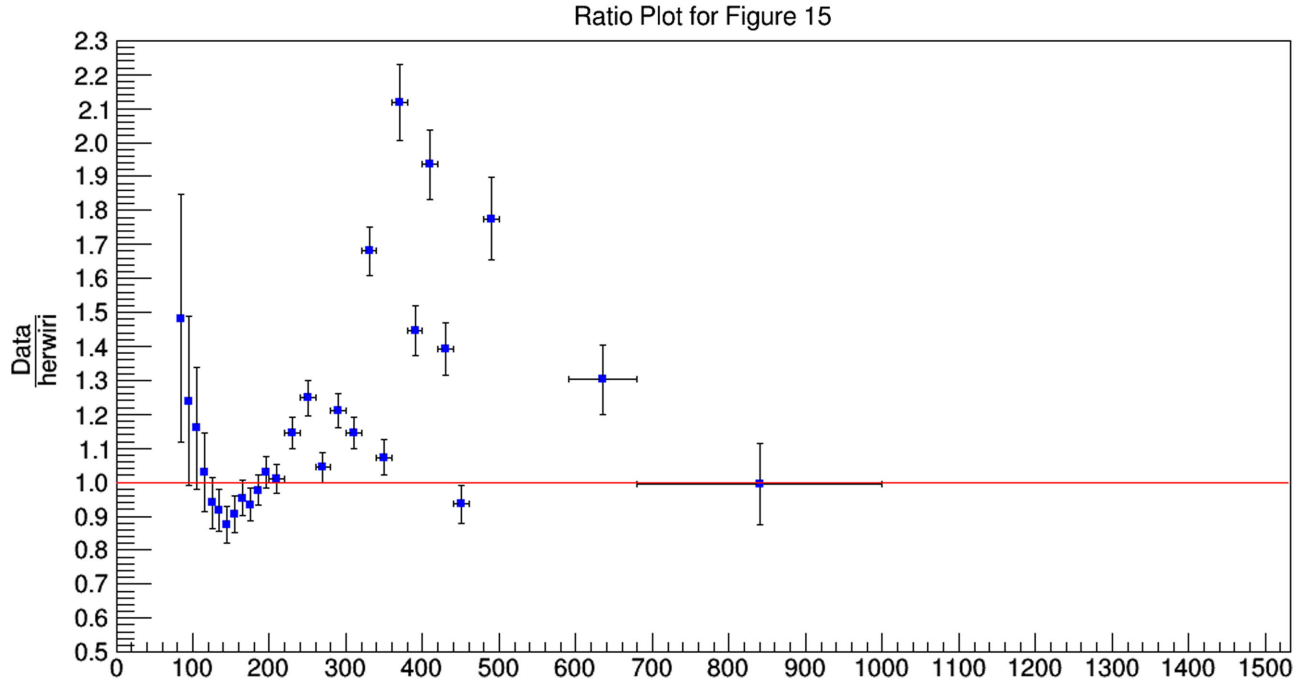

FIG. 47. Ratio plot for the production of $W +$ jets as a function of the scalar sum H_T in $N_{\text{jet}} = 1$. The data are divided by predictions from MADGRAPH5_aMC@NLO/HERWIRI1.031.

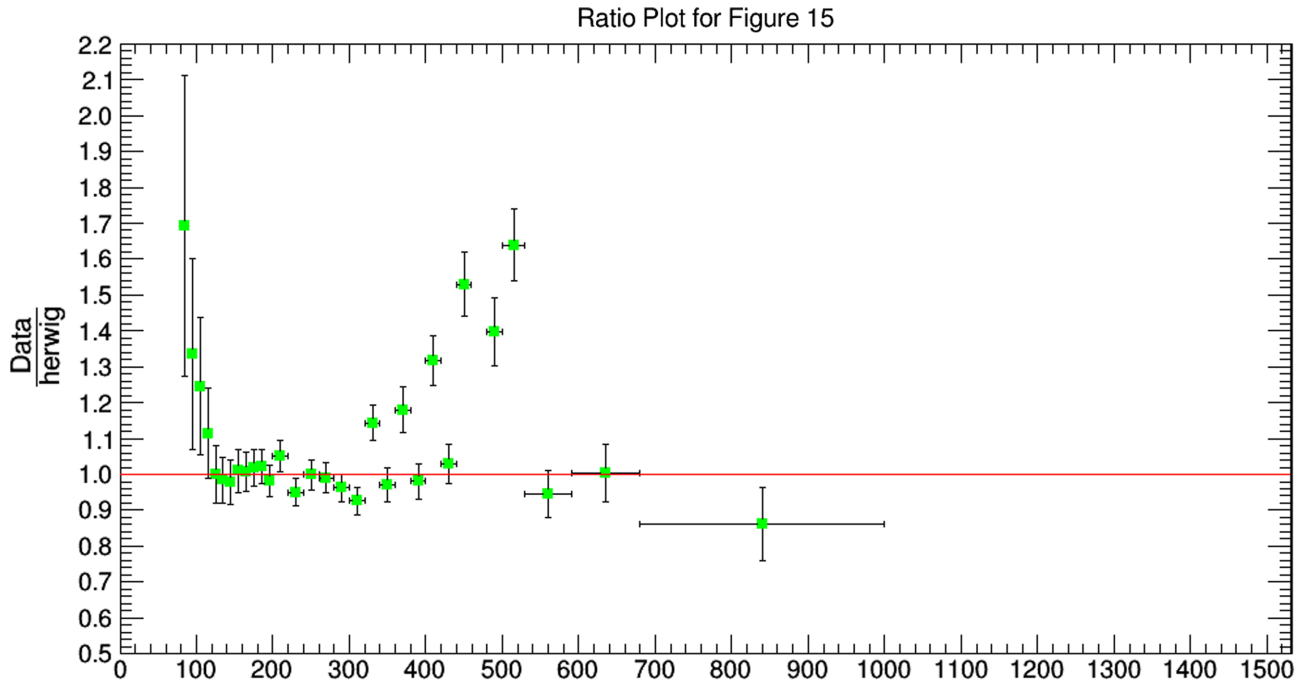

FIG. 48. Ratio plot for the production of $W+$ jets as a function of the scalar sum H_T in $N_{\text{jet}} = 1$. The data are divided by predictions from MADGRAPH5_aMC@NLO/HERWIG6.521.

APPENDIX D: ERROR PLOTS

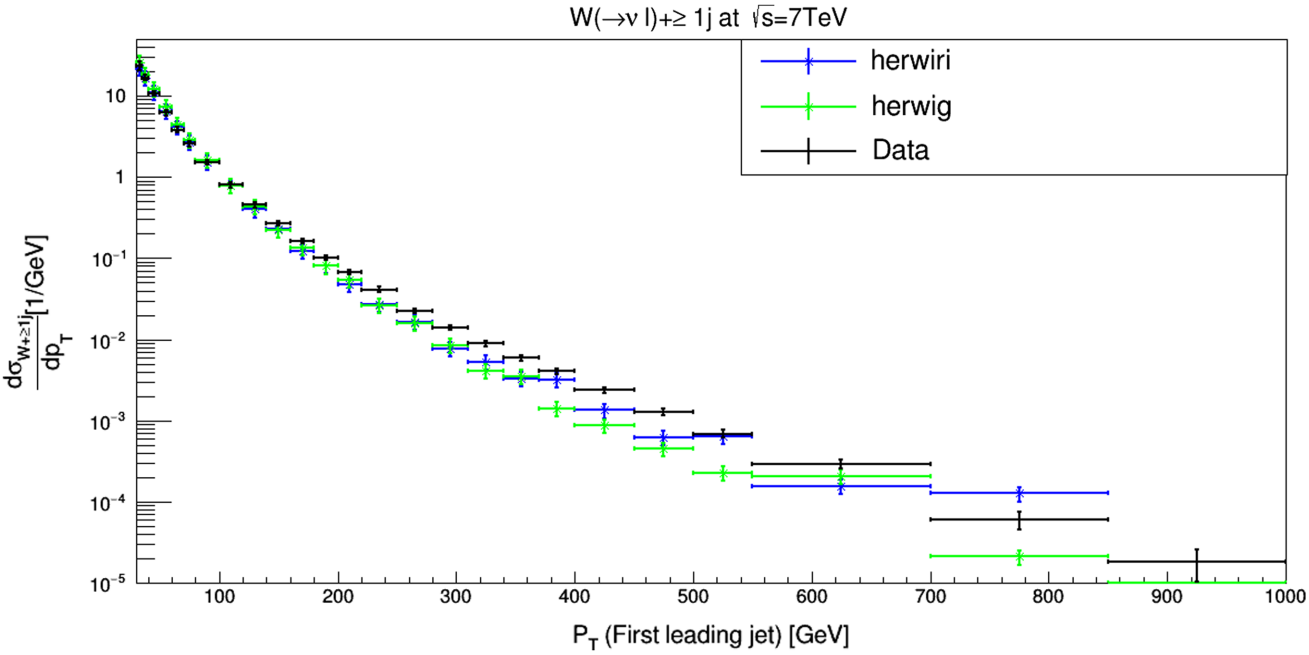

FIG. 49. Cross section for the production of $W+$ jets as a function of the leading-jet P_T in $N_{\text{jet}} \geq 1$. The data are compared to predictions from MADGRAPH5_aMC@NLO/HERWIRI1.031 and MADGRAPH5_aMC@NLO/HERWIG6.521. The 20% theoretical errors are shown for illustration.

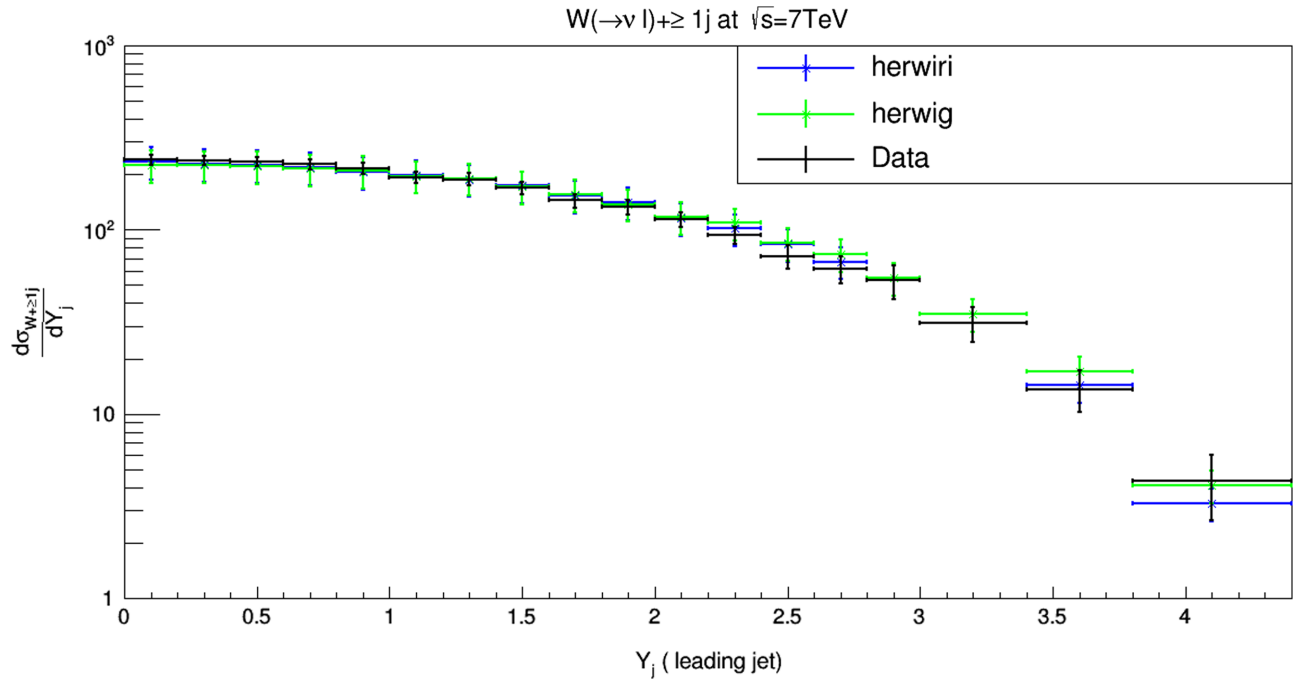

FIG. 50. Cross section for the production of $W+$jets as a function of the leading-jet Y_j in $N_{\text{jet}} \geq 1$. The data are compared to predictions from MADGRAPH5_aMC@NLO/HERWIRI1.031 and MADGRAPH5_aMC@NLO/HERWIG6.521. The 20% theoretical errors are shown for illustration.

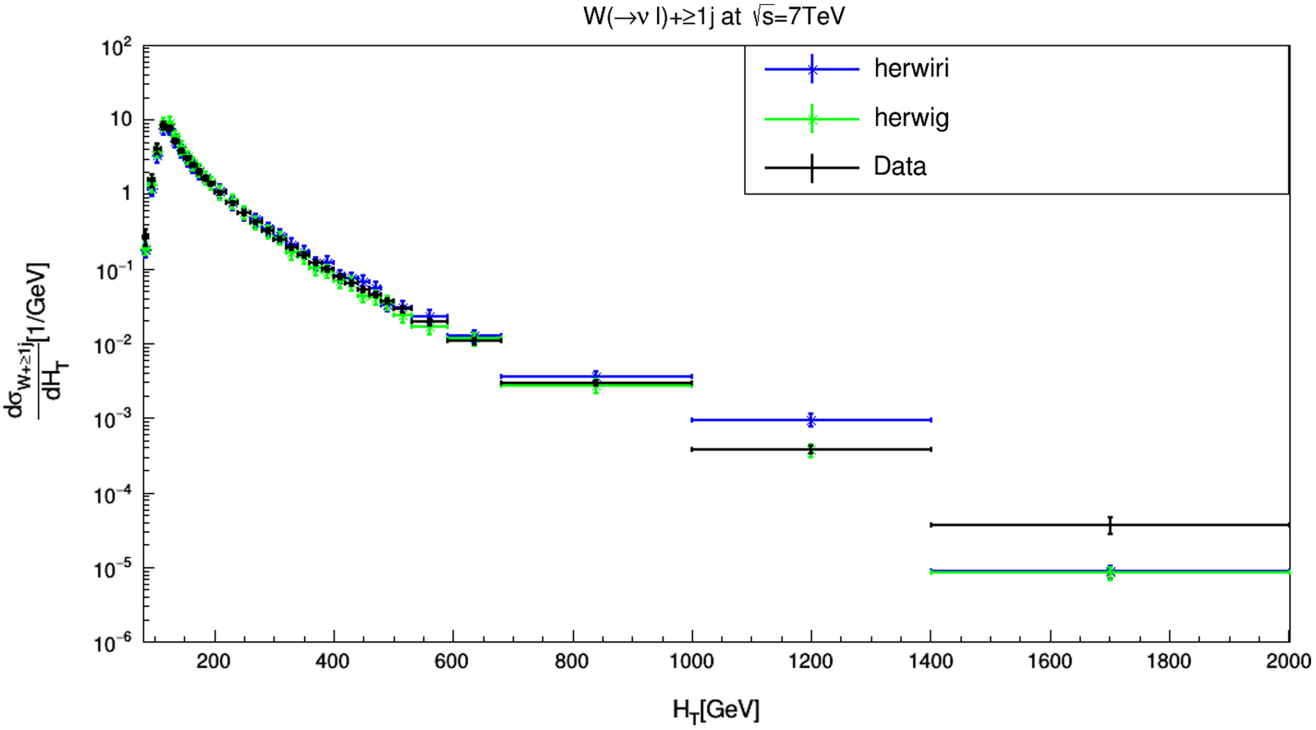

FIG. 51. Cross section for the production of $W+$jets as a function of the scalar sum H_T in $N_{\text{jet}} \geq 1$. The data are compared to predictions from MADGRAPH5_aMC@NLO/HERWIRI1.031 and MADGRAPH5_aMC@NLO/HERWIG6.521. The 20% theoretical errors are shown for illustration.

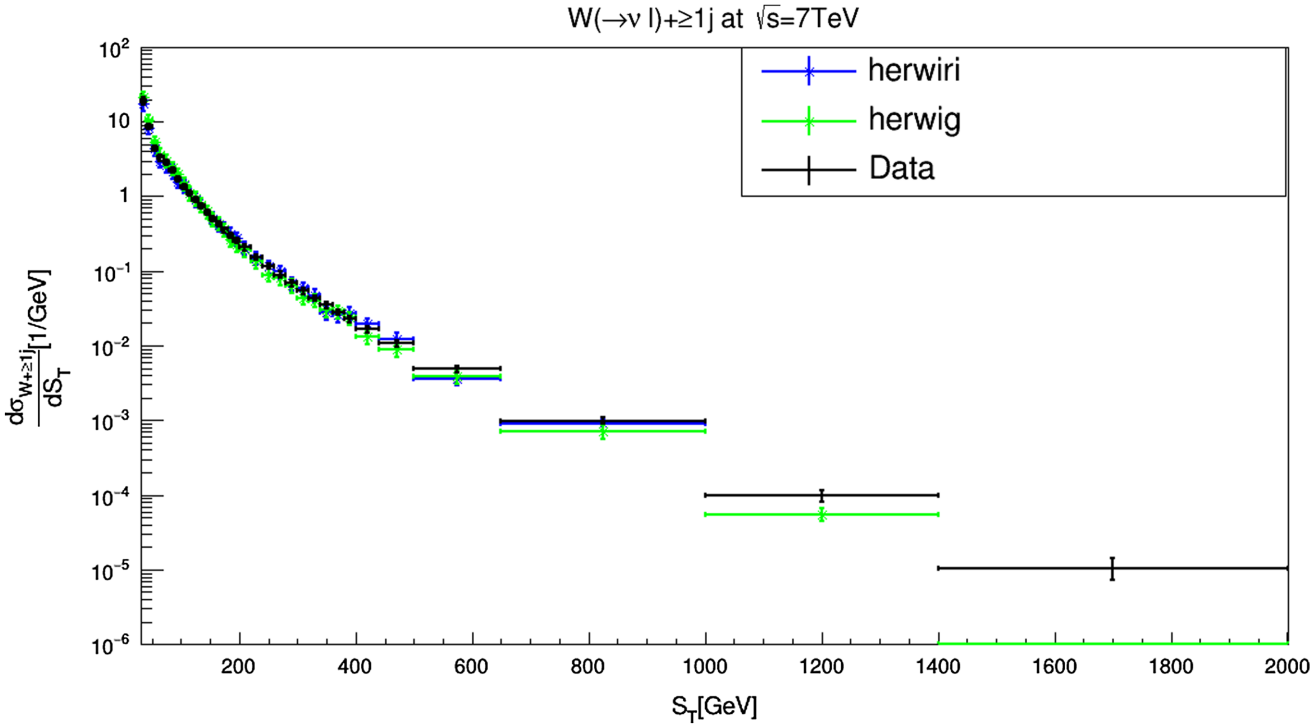

FIG. 52. Cross section for the production of $W+$ jets as a function of the scalar sum S_T in $N_{\text{jet}} \geq 1$. The data are compared to predictions from MADGRAPH5_aMC@NLO/HERWIRI1.031 and MADGRAPH5_aMC@NLO/HERWIG6.521. The 20% theoretical errors are shown for illustration.

[1] G. 't Hooft and M. J. G. Veltman, Regularization and renormalization of gauge fields, Nucl. Phys. **B44**, 189 (1972).

[2] G. 't Hooft, Renormalizable Lagrangians for Massive Yang-Mills Fields, Nucl. Phys. **B35**, 167 (1971).

[3] G. t Hooft, Renormalization of massless Yang-Mills fields, Nucl. Phys. **B33**, 173 (1971).

[4] F. Bloch and A. Nordsieck, Note on the radiation field of the electron, Phys. Rev. **52**, 54 (1937).

[5] D. R. Yennie, S. C. Frautschi, and H. Suura, The infrared divergence phenomena and high-energy processes, Ann. Phys. (N.Y.) **13**, 379 (1961).

[6] G. Grammer, Jr. and D. R. Yennie, Improved treatment for the infrared divergence problem in quantum electrodynamics, Phys. Rev. D **8**, 4332 (1973).

[7] B. F. L. Ward, IR-improved operator product expansions in non-Abelian gauge theory, Mod. Phys. Lett. A **28**, 1350069 (2013) [**28**, 1350069 (2013)].

[8] B. F. L. Ward, IR-improved DGLAP theory: Kernels, parton distributions, reduced cross sections, Ann. Phys. **323**, 2147 (2008).

[9] B. F. L. Ward, Ir-improved DGLAP theory, Adv. High Energy Phys. **2008**, 682312 (2008).

[10] G. Altarelli and G. Parisi, Asymptotic freedom in parton language, Nucl. Phys. **B126**, 298 (1977).

[11] Y. L. Dokshitzer, Calculation of the structure functions for deep inelastic scattering and $e+e-$ annihilation by perturbation theory in quantum chromodynamics, Zh. Eksp. Teor. Fiz. **73**, 1216 (1977) [Sov. Phys. JETP **46**, 641 (1977)].

[12] V. N. Gribov and L. N. Lipatov, $e+e-$ pair annihilation and deep inelastic e p scattering in perturbation theory, Yad. Fiz. **15**, 1218 (1972) [Sov. J. Nucl. Phys. **15**, 675 (1972)].

[13] J. C. Collins and J. w. Qiu, A new derivation of the Altarelli-Parisi equations, Phys. Rev. D **39**, 1398 (1989).

[14] B. F. L. Ward and S. A. Yost, HERWIRI1.031: New approach to parton shower MCs in precision QCD theory, *Proc. Sci.*, ICHEP2010 (2010) 127.

[15] B. F. L. Ward, S. Joseph, S. Majhi, and S. A. Yost, MC realization of IR-improved DGLAP-CS parton showers: HERWIRI1.0, *Proc. Sci.*, RADCOR2009 (2010) 070 [Mod. Phys. Lett. A **25**, 2207 (2010)].

[16] S. Joseph, S. Majhi, B. F. L. Ward, and S. A. Yost, New approach to parton shower MCs for precision QCD theory: HERWIRI 1.0(31), Phys. Rev. D **81**, 076008 (2010).

[17] S. Joseph, S. Majhi, B. F. L. Ward, and S. A. Yost, HERWIRI1.0: MC realization of IR-improved DGLAP-CS parton showers, Phys. Lett. B **685**, 283 (2010).

[18] S. K. Majhi, A. Mukhopadhyay, B. F. L. Ward, and S. A. Yost, Phenomenological study of the interplay between

IR-Improved DGLAP-CS theory and the precision of an NLO ME matched parton shower MC, Ann. Phys. (Amsterdam) **350**, 485 (2014).

[19] S. K. Majhi, A. Mukhopadhyay, B. F. L. Ward, and S. A. Yost, Phenomenology of the interplay between IR-improved DGLAP-CS theory and NLO ME matched parton shower MC precision, Phys. Lett. B **719**, 367 (2013).

[20] A. Mukhopadhyay and B. F. L. Ward, Interplay between IR-improved DGLAP-CS theory and the precision of an NLO ME matched parton shower MC in relation to LHCb data, Mod. Phys. Lett. A **31**, 1650063 (2016).

[21] J. Alwall, R. Frederix, S. Frixione, V. Hirschi, F. Maltoni, O. Mattelaer, H.-S. Shao, T. Stelzer, P. Torrielli, and M. Zaro, The automated computation of tree-level and next-to-leading order differential cross sections, and their matching to parton shower simulations, J. High Energy Phys. 07 (2014) 079.

[22] G. Corcella, I. G. Knowles, G. Marchesini, S. Moretti, K. Odagiri, P. Richardson, M. H. Seymour, and B. R. Webber, HERWIG 6: An event generator for hadron emission reactions with interfering gluons (including supersymmetric processes), J. High Energy Phys. 01 (2001) 010.

[23] B. F. L. Ward and S. A. Yost, QED x QCD resummation and shower/ME matching for LHC physics, Acta Phys. Pol. B **38**, 2395 (2007).

[24] B. F. L. Ward and S. A. Yost, New developments in precision LHC theory: QED x QCD exponentiation, shower/ME matching, IR-improved DGLAP-CS theory and implications for UV finite quantum gravity, *Proc. Sci.*, RADCOR2007 (2007) 038.

[25] B. F. L. Ward, S. Joseph, S. Majhi, and S. A. Yost, Precision QED x QCD resummation theory for LHC physics: IR-improved scheme for parton distributions, kernels, reduced cross sections with shower/ME matching, arXiv:0810.0723.

[26] B. F. L. Ward, C. Glosser, S. Jadach, and S. A. Yost, Threshold corrections in precision LHC physics: QED x QCD, Int. J. Mod. Phys. A **20**, 3735 (2005).

[27] B. F. L. Ward, C. Glosser, S. Jadach, and S. A. Yost, Threshold corrections in QED x QCD at the LHC, arXiv: hep-ph/0410277.

[28] D. B. DeLaney, S. Jadach, C. Shio, G. Siopsis, and B. F. L. Ward, Multiple gluon effects in fermionanti-fermion scattering at SSC/CERN LHC energies, Phys. Rev. D **52**, 108 (1995).

[29] D. B. DeLaney, S. Jadach, C. Shio, G. Siopsis, and B. F. L. Ward, Renormalization group improved exponentiation of soft gluons in QCD, Phys. Lett. B **342**, 239 (1995).

[30] B. F. L. Ward and S. Jadach, YFS MC approach to QCD soft gluon exponentiation, Acta Phys. Pol. B **33**, 1543 (2002).

[31] B. F. L. Ward, Renormalization group improved Yennie-frautschi-suura theory, Phys. Rev. D **36**, 939 (1987).

[32] R. K. Ellis, H. Georgi, M. Machacek, H. D. Politzer, and G. G. Ross, Perturbation theory and the parton model in QCD, Nucl. Phys. **B152**, 285 (1979).

[33] S. Joseph, S. Majhi, B. F. L. Ward, and S. A. Yost, New approach to parton shower MCs for precision QCD theory: HERWIRI 1.0(31), Phys. Rev. D **81**, 076008 (2010).

[34] R. D. Ball *et al.*, Parton distributions with LHC data, Nucl. Phys. **B867**, 244 (2013).

[35] Note that only the showers are IR-improved in Herwiri1.031 and that, since this affects terms starting at $O(\alpha_s^2 L)$, exactness at $O(\alpha_s)$ is unaffected in MADGRAPH5_aMC@NLO/Herwiri1.031.

[36] We will see later that HERWIRI gives either a better fit to the data or an acceptable fit without this extra intrinsic Gaussian kick.

[37] M. Cacciari, G. P. Salam, and G. Soyez, FastJet User Manual, Eur. Phys. J. C **72**, 1896 (2012).

[38] G. Aad *et al.* (ATLAS Collaboration), Measurements of the W production cross sections in association with jets with the ATLAS detector, Eur. Phys. J. C **75**, 82 (2015).

[39] The rapidity term in $\Delta R = \sqrt{\Delta\phi^2 + \Delta Y^2}$ is often replaced by pseudorapidity if the involved particles are massless.

[40] V. Khachatryan *et al.* (CMS Collaboration), Differential cross section measurements for the production of a W boson in association with jets in proton–proton collisions at $\sqrt{s} =$ 7 TEV, Phys. Lett. B **741**, 12 (2015).